



FACULTY OF INFORMATION TECHNOLOGY AND ELECTRICAL ENGINEERING  
DEGREE PROGRAMME IN ELECTRONICS AND COMMUNICATIONS ENGINEERING

# MASTER'S THESIS

**POWER BEACONS DEPLOYMENT OPTIMIZATION FOR  
WIRELESSLY POWERING MASSIVE INTERNET OF THINGS  
NETWORKS**

Author	Osmel Martínez Rosabal
Supervisor	Assist. Prof. Hirley Alves
Second Examiner	Assist. Prof. Onel López
Technical Advisor	Prof. Samuel Montejo

February 2021

Martínez Rosabal O. (2021) Power beacons deployment optimization for wirelessly powering massive Internet of Things networks. University of Oulu, Degree Programme in Electrical Engineering, 61 p.

## ABSTRACT

The fifth-generation (5G) and beyond wireless cellular networks promise the native support to, among other use cases, the so-called Internet of Things (IoT). Different from human-based cellular services, IoT networks implement a novel vision where ordinary machines possess the ability to autonomously sense, actuate, compute, and communicate throughout the Internet. However, as the number of connected devices grows larger, an urgent demand for energy-efficient communication technologies arises. A key challenge related to IoT devices is that their very small form factor allows them to carry just a tiny battery that might not be even possible to replace due to installation conditions, or too costly in terms of maintenance because of the massiveness of the network. This issue limits the lifetime of the network and compromises its reliability.

Wireless energy transfer (WET) has emerged as a potential candidate to replenish sensors' batteries or to sustain the operation of battery-free devices, as it provides a controllable source of energy over-the-air. Therefore, WET eliminates the need for regular maintenance, allows sensors' form factor reduction, and reduces the battery disposal that contributes to the environment pollution.

In this thesis, we review some WET-enabled scenarios and state-of-the-art techniques for implementing WET in IoT networks. In particular, we focus our attention on the deployment optimization of the so-called power beacons (PBs), which are the energy transmitters for charging a massive IoT deployment subject to a network-wide probabilistic energy outage constraint. We assume that IoT sensors' positions are unknown at the PBs, and hence we maximize the average incident power on the worst network location. We propose a linear-time complexity algorithm for optimizing the PBs' positions that outperforms benchmark methods in terms of minimum average incident power and computation time. Then, we also present some insights on the maximum coverage area under certain propagation conditions.

**Keywords:** deployment optimization algorithm, massive IoT, minimum incident power, power beacons, wireless energy transfer.

# TABLE OF CONTENTS

ABSTRACT	
TABLE OF CONTENTS	
FOREWORD	
LIST OF ABBREVIATIONS AND SYMBOLS	
1 INTRODUCTION	8
1.1 Energy-efficient communications.....	8
1.2 Energy harvesting from ambient sources .....	10
1.3 Electromagnetic-based WET.....	12
1.4 Thesis contribution .....	13
1.5 Thesis outline .....	14
2 RF WIRELESS ENERGY TRANSFER	15
2.1 Multi-antenna WET scenarios .....	18
2.1.1 On the CSI estimation for WET .....	19
2.2 Wireless powered communication networks .....	20
2.2.1 Cooperative WPCNs .....	22
2.2.2 Power control protocols in WPCNs .....	23
2.2.3 Ambient EH-assisted WPCNs .....	23
2.3 Simultaneous wireless information and power transfer .....	24
2.4 Health concerns about WET.....	26
2.5 Optimization deployment of energy and information transmitters .....	27
3 PBS DEPLOYMENT FOR MASSIVE WET	30
3.1 System model .....	30
3.2 Problem formulation.....	31
3.3 On the optimal PBs' positions.....	32
3.3.1 Equally-far-from-Center approach (EC) .....	32
3.3.2 Interior Point Method approach (IPM) .....	37
3.3.3 Nature-inspired meta-heuristic approaches .....	39
3.4 Algorithm for optimal deployment and practical considerations .....	42
4 NUMERICAL RESULTS	44
4.1 On the optimal PBs' positions.....	44
4.2 On the optimal solutions of <b>P1</b> .....	45
4.3 On the maximum coverage area .....	47
4.4 On CSI-free multi-antenna WET .....	48
5 CONCLUSIONS	51
6 REFERENCES	52

## FOREWORD

This thesis focuses on the deployment of PBs for powering a massive IoT under QoS requirements. This work was conducted as part of the MOSSAF project at the Centre for Wireless Communications (CWC) of the University of Oulu, Finland.

Being at the University of Oulu has been one of the greatest experiences in my whole life as it allowed me to discover the fascinating world of research. For this reason, I would like to thank everyone that has made possible this journey. First, I would like to thank Assistant Professor Onel López for his support since I arrived at Oulu and for his unconditional friendship, especially in very sad moments. Also, to Assistant Professor Hirley Alves for allowing me to work at the Machine-type Communications group, for his constant guidance in the research world, and for his tutorials on "how to make a great espresso". To Professor Samuel Montejo for constantly supporting my research work, and for his valuable advises that helped me grow professionally.

I would like to thank all my Cuban friends Lisi, Dian, Nelson and the rest of the colleges at the CWC for all the great moments. Also, to my girlfriend Patricia for her love and guidance in Finnish matters.

Special thanks to my beloved mom Oraima, for making a great effort to raise and educate me, my sister Daidee for being at my side all the time, and my grandparents "Tito" and "Tita" for their infinite love.

I would like to dedicate this work to my little princess Laura, my daughter, who is my source of inspiration and strength. I hope that one day you follow daddy's steps.

This research has been financially supported by Academy of Finland, 6Genesis Flagship (Grant n.318927) and EE-IoT (n.319008).

Oulu, 11th March, 2021

Osmel Martínez Rosabal

## LIST OF ABBREVIATIONS AND SYMBOLS

### Abbreviations:

AF	Amplify-and-forward
AS	Antenna switching
BS	Base station
CSI	Channel state information
CSIT	CSI at the transmitter
DAS	Distributed antenna system
DC	Direct current
DF	Decode-and-forward
DPS	Dynamic PS
EC	Equally-far-from-center PBs' deployment
EH	Energy harvesting
EMF	Electromagnetic field
FB-FTT	Finite blocklength-FTT
FB-FTUT	Finite blocklength fixed threshold uninterrupted transmission
FTT	Fixed threshold transmission protocol
GAs	Genetic algorithms
HAP	Hybrid access point
HTT	Harvest-then-transmit protocol
ID	Information decoding
IoT	Internet of Things
IPM	Interior-point methods
LoS	Line-of-sight
MIMO	Multiple-input multiple-output
mmWave	Millimeter waves
NLoS	Non LoS
Ode-PoBes	Optimal DEployment of POver BEaconS algorithm
PB	Power beacon
PS	Power Splitting
PSO	Particle swarm optimization
QoS	Quality-of-service
RF	Radio frequency
SIMO	Single-input multiple-output
SINR	Signal-to-interference-plus-noise ratio
SISO	Single-input single-output
SNR	Signal-to-noise ratio
SWIPT	Simultaneous wireless information and power transfer
TS	Time switching
UAV	Unmanned aerial vehicle
WET	Wireless energy transfer
WIT	Wireless information transfer
WPCN	Wireless-powered communications network

### Symbols:

$\mathcal{S}$	set of IoT sensors
$\mathcal{B}$	set of PBs
$\mathcal{Q}$	set of particles in the PSO framework
$A$	number of antennas at each PB
$S_s$	$s^{\text{th}}$ sensor in the set $\mathcal{S}$
$PB_b$	$b^{\text{th}}$ PB in the set $\mathcal{B}$
$q$	$q^{\text{th}}$ particle in the set $\mathcal{Q}$
$h_{s,b}$	complex channel coefficient of the $PB_b \rightarrow S_s$ link
$\alpha, \beta$	real and imaginary parts of $h_{s,b}$ respectively
$\varrho_{s,b}$	path-loss function of the $PB_b \rightarrow S_s$ link
$d_{s,b}$	distance of the $PB_b \rightarrow S_s$ link
$P, P_T$	PB transmit power and total transmit power respectively
$\kappa$	Rician fading factor
$\gamma$	path-loss exponent
$K$	unitless constant for the path-loss model
$x_b$	energy-carrying signal transmitted from $PB_b$
$\xi_s^{\text{RF}}$	incident RF power at the $s^{\text{th}}$ sensor
$\xi_0$	sensitivity of the EH's circuitry
$\zeta$	energy outage probability threshold
$R$	radius of the coverage area
$T_{\text{avg}}$	normalized average computational time
$\boldsymbol{\lambda}$	Lagrange multiplier vector for equality constraints, $\boldsymbol{\lambda} = \{\lambda_b\}$
$\mathbf{t}$	slack variable for the inequality constraints, $\mathbf{t} = \{t_b\}$
$\mu$	barrier parameter in the IPM framework
$r$	PBs' distance to the center in the EC deployments (optimal value $r^*$ )
$\theta$	angular separation between adjacent PBs in the EC deployments (optimal value $\theta^*$ )
$\Delta r$	step size in the Ode-PoBes algorithm
$s^*$	index of the sensor with the minimum average incident power
$\epsilon$	barrier parameter in the PSO framework
$\mathbf{z}_{q,i,b}$	2D Cartesian coordinates of the $b^{\text{th}}$ PB in the $q^{\text{th}}$ particle at the $i^{\text{th}}$ iteration
$\mathbf{n}_b$	2D Cartesian coordinates of the $b^{\text{th}}$ PB

### Mathematical Notation:

$\mathbb{C}$	set of complex numbers
$\mathbb{N}$	set of natural numbers
$\mathbb{E}_x[\cdot]$	expectation with respect to the random variable $x$
$\mathbb{I}[\cdot]$	indicator function, which is 0 whenever the argument is nonpositive and $+\infty$ otherwise
$\mathcal{L}(\cdot)$	Lagrangian of an optimization problem
$\mathcal{O}(\cdot)$	big-O notation for specifying the worst-time complexity of an algorithm
$\max_x f(\cdot)$	maximum of $f(\cdot)$ over $x$

$\min_x f(\cdot)$	minimum of $f(\cdot)$ over $x$
$\arg \max_x f(\cdot)$	value of $x$ that maximizes $f(\cdot)$
$\lfloor \cdot \rfloor$	round down to the next integer
$ \cdot $	absolute value for scalars, or cardinality when a set is in the argument
$\ \cdot\ _p$	$\ell_p$ -norm operator defined as $\ \mathbf{x}\ _p = (\sum_{\forall i}  x_i^p )^{1/p}$

# 1 INTRODUCTION

The Internet of Things (IoT) defines a novel paradigm that brings connectivity to an increasing number of physical objects for sensing and interacting with the surrounding environment. IoT technologies impact all spheres of society and life creating new business opportunities, collecting a huge amount of data to help decisions, and improving healthcare systems just to mention a few. By 2030, tens of billions of deployed devices are foreseen to serve a variety of use cases—e.g. environmental monitoring, home automation, smart agriculture, remote health care and industry 4.0—with heterogeneous quality-of-service (QoS) requirements and hardware implementations [1]. Key enablers for boosting IoT are the fifth generation (5G) and beyond cellular networks that promise the native support to ultra-reliable and low-latency communications, extreme mobile broadband and massive machine-type communications. The way each of these services will impact IoT networks depends on the particular application.

Among others, a big challenge in IoT networks is that devices are usually of small form-factor and can carry just a tiny battery, thus the energy availability is limited and compromises devices' lifetime. Besides, battery replacements and manual charging are often impractical if not forbidden due to the hard-to-reach installation conditions or the massive number of sensors. Imagine thousands of low-power devices with heterogeneous energy demands running out of battery, it may cause constant service interruptions plus the unaffordable cost/time of maintenance. Moreover, inappropriate battery recycling and fossil fuel electricity generation contribute to water and air pollution as their toxic chemical residuals are released into the environment. Therefore, energy efficiency solutions promote environmentally-friendly products and services and make the telecommunications sector a more profitable business since energy costs constitute almost half of the operating expenses [2]. Hence, we need green technologies to sustain future IoT networks with minimum energy consumption and waste generation, and to increase customer satisfaction due to prolonged battery life. Current wireless networks lack of consistent infrastructure for enabling green technologies [3]; however, there are already some energy-efficient wireless standards available in the market, such as ZigBee [4], Bluetooth low energy (BLE) [5], IPv6 over low-power wireless personal area networks (6LoWPAN) [6], IEEE 802.15.6 [7], and Message Queuing Telemetry Transport (MQTT) [8].

## 1.1 Energy-efficient communications

The concept of sustainable IoT encompasses five domains: radio optimization, data reduction, sleep/wake-up schemes, energy-efficient routing algorithms, and battery repletion [9], [3]. Since the radio interface is the most power-hungry module, its optimization can significantly alleviate the battery drain issue. One thing to consider is that IoT traffic is mostly sporadic with long periods of inactivity; hence, duty-cycling techniques can reduce the idle-listening periods which maximize the network lifetime. But, targeting very low duty cycles may increase significantly the end-to-end message delay in multihop networks, plus the usual non-deterministic delay due to the different communication paths. Designers must also consider that reducing the transmission/reception windows potentially increases the collision rate and adds



extra control traffic overhead for synchronization [10]. Another way to reduce energy consumption during idle-listening periods is with a low-power wake-up radio (WUR). A WUR monitors the channel searching for pre-assigned wake-up commands to activate the main transceiver. State-of-the-art WUR can achieve -71 dBm of sensitivity with 7.6 nW of total consumption [11]. The design of WUR raises a trade-off among the sensitivity level, communication range, robustness against interference while keeping the power consumption negligible in comparison with the main components. Moreover, modulation optimization aims to find the optimal constellation considering the trade-off between constellation size, information rate, transmission time, link distance, and noise/interference levels.

Meanwhile, note that significant performance gains may come from using directional antennas. Directional antennas do not just increase the coverage but also improve the energy-efficiency of the network. Different from the omnidirectional implementation, directional antennas focus the energy towards the devices, which reduces the level of interference and improves the signal-to-noise ratio (SNR), and therefore, directional antennas can improve reliability and reduce the number of retransmissions. Similarly, base stations (BSs) equipped with multiple antennas can steer sharp beams towards multiple devices at the same time, allowing the separation of multiple streams. However, optimal beamforming strategies require accurate channel state information (CSI) acquisition which consumes an important portion of the devices' energy budget [12].

On the other hand, heterogeneous QoS specifications and hardware design cause different power consumption profiles within an IoT network. In such scenarios, adaptive power allocation strategies allow each sensor to adjust its transmit power according to the battery state, level of interference, data rate, just to mention a few [13]. Power allocation algorithms can be either centralized at the BSs or distributed [14]. In the former, the BS computes the appropriate sensors' transmit power and forward the resource allocation decisions to the devices, saving a computation overhead at each low-cost device. In the case of distributed algorithms, each device computes the optimal power allocation strategy based on the CSI provided by neighbouring devices. Hence, distributed algorithms offer a more practical approach as the number of devices increases, since estimating the CSI at the BS could be unattainable. Cooperation is another energy-efficient solution since sensors with the best channel conditions can forward its neighbour's packets to the final destination [15]. It saves energy in the far away sensors in addition to extending the coverage area. Nevertheless, cooperation can increase the end-to-end delay as the number of intermediate steps increases. Energy-aware routing protocols consider the remaining energy at each sensor in the network to discover feasible communication paths (e.g. the energy-efficient ad-hoc on-demand distance vector protocol) [16]. These protocols input multiple entries in the routing tables pointing to the same destination, which reduces the recovery time against faults. Moving BS, such as unmanned aerial vehicles (UAVs), reduces the link distance and avoid multi-hop transmissions; hence they are suitable candidates for many coming IoT use cases.

Additionally, note that the energy consumption of the radio interface is an increasing function of the size and number of packets. Instead of sending raw measurements, a sensor can extract some statistics or compress the information before transmit it to reduce the time-on-air [17]. For instance, we may be interested in the number of times an event has happened, the average temperature in a room, or the maximum humidity

level in a warehouse, instead of all measurements, thus instantaneous measure reporting could be avoided. The reader must keep in mind that these techniques reduce the accuracy of the data and demand more computational effort from the sensor devices. Moreover, continuous sensing operations also consumes energy, while an efficient sensing approach may take into account that measurements are often time-correlated. Hence, compressing the sensing itself would not only reduce the size of the transmitted data but also prolong the network lifetime [18]. In other scenarios, the sensors' positions generate spatial correlation in the received data at the sink. This redundancy can be eliminated by turning off the redundant sensors or adapting its sampling rate [19]. In multi-hop networks, sending individual packets from the BS increases unnecessarily the number of transmissions. Instead, by using linear network coding the BS can send a linear combination of the packets for each end-user to decode its information by solving a system of linear equations [20].

Finally, energy harvesting (EH) is a promising candidate for recharging sensors' batteries without human intervention. It allows the sensors to turn alternative sources of energy into electricity for supporting their operation and extend the network lifetime. Meanwhile, wireless energy transfer (WET) utilizes dedicated energy transmitters to replenish the sensor's batteries or to support zero-battery IoT networks. In the following sections, we discuss more these approaches.

## 1.2 Energy harvesting from ambient sources

In our surroundings, there are numerous renewable sources of energy that may be suitable for supporting the operation of IoT networks. For instance, photovoltaic cells turn the sunlight into electricity thanks to the photovoltaic effect. The transformation takes place when a semiconductor is exposed to the sunlight and the absorbed photons cause the electrons to cross the p-n junction, which then produces an electric current. However, the sunlight intensity depends on the atmospheric conditions and the geographic place, which makes the energy arrival process almost unpredictable. The output power of a photovoltaic cell is also a function of its temperature and the characteristics of the load; hence, solar-powered systems utilize maximum power point tracking techniques (although it applies for other sources, this technique is more frequently used with solar panels) to ensure maximum transfer efficiency to the load [21]. Alternatively, it is possible to exploit artificial lights within indoor environments to sustain the operation of the sensors. Nevertheless, artificial lights are weaker than the sunlight; their availability is restricted to the offices' schedule.

On the other hand, thermoelectric generators are solid-state devices capable of producing electricity from thermal energy. The gradients of temperature near to the dissimilar thermoelectric materials cause an output voltage due to the thermoelectric effects, and on the contrary, when a voltage is applied it creates a temperature difference [22]. The reliable design of thermoelectric generators (e.g., non-moving parts, orientation independent installation/operation) makes them suitable for applications in severe environments where regular maintenance is impossible. Typical applications range from powering sensors inside the moving parts of hydroelectric turbines [23], monitor the temperature of walls and pipes in dark chambers in absence of airflow [24], and aerospace industry.

Piezoelectric-based energy harvesters generate electricity after being exposed to mechanical strain-stress, vibration or the motion of the human activity thanks to the so-called piezoelectric effect. However, the electrical signal at the output of the generator has a high-peak voltage and a very low current which reduce conversion efficiency of the regulation circuit. Similarly, electrostatic-based EH uses the mechanical motion and vibration to change the plate separation of a capacitor against an electric field to generate electricity; but, to operate they require a polarization source or a special dielectric material which complicates the design. These devices can be utilized to power wearable electronics, in vibrating structures such as roads, and to power tracking sensor for monitoring the animal activity [25].

Wind-based EH systems can sustain wireless networks in remote zones with lack of power grid infrastructure. The wind turbines convert the kinetic energy of the wind into electricity whose power is proportional to the cube of the wind speed. The wind speed can be statistically characterized with the Weibull distribution, which provides useful insights for estimating the probability of outage in wind-powered wireless networks [26]. Nevertheless, wind-based EH is not suitable to be incorporated in the IoT devices themselves, but on the BSs or access points (APs). Also, different from large-scale wind systems, small-scale designs for IoT devices exhibit a low efficiency due to very low flow rates and fluctuations in the wind speed [27].

In the cities, EH from ambient radio-frequency (RF) stands out from renewable harvesting solutions provided the availability of RF signals coming from TV transmitters, WiFi APs, cellular networks, radio broadcast stations, among others. RF-based EH recycles the energy coming from human-made transmitters by using a rectifier circuit [28], which reduces the size and complexity of the IoT devices compared with other ambient EH implementations. However, the energy density values available at the RF-EH receivers are typically too low, thus limiting the amount of harvestable energy.

The authors in [29] surveyed London to find potential sources for RF-EH. They were interested in the power density nearby: digital TV (DTV) transmitters; GSM900, GSM1800, and 3G BSs; and WiFi APs. They found that the DTV signals strength heavily depends on line-of-sight (LoS) and changes rapidly according to atmospheric conditions, whereas the user traffic conditions WiFi signal level stability. Moreover, vertically polarized antennas at the cellular BSs constrain the orientation of the IoT sensors. Similarly, the authors in [30] recorded values of -30 to -15 dBm of peak power at a few hundred meters from UHF DTV towers in Tokyo, Japan. Measurements campaigns in Calgary, Canada, in cellular bands (824-960 MHz, 1710-2170 MHz) and the unlicensed industrial, scientific, and medical band, reported power peak values of -30 to -20 dBm [31].

Ambient RF-EH is considered extremely challenging as RF power density varies with time, frequency and distance to the transmitter within the range of  $0.0002 \sim 1 \mu\text{W}/\text{cm}^2$  [30]. Some researches have proposed different alternatives to boost the harvested energy. For instance, in [32] the authors proposed a packet injection algorithm for artificial traffic generation in WiFi networks to reduce the silent periods of the WiFi APs. Such mechanism allowed reaching a receive power in the range of -23 to -5 dBm with a separation from the router of 50 cm and almost with full efficiency of the EH circuit. In [33], the authors designed a multiband RF-EH system to combine the signals coming from multiple wireless systems. The designed EH circuit operates when the input power is between -25 to -5 dBm and with a maximum efficiency of 33 % at 2100 MHz. This solution

Table 1. Comparison of EH techniques [34–36]

Source	EH technology	Power density	Main shortcomings
Sunlight	Photovoltaic cells	100 mW/cm <sup>2</sup>	sensitive to blockage
Indoor light	Photovoltaic cells	83 $\mu$ W/cm <sup>2</sup>	sensitive to blockage and very low conversion efficiency
Thermal	Termoelectric generators	1 mW/cm <sup>2</sup>	low conversion efficiency, costly, and heavy
Kinetic	Piezoelectric effect	0.3 mW/cm <sup>3</sup>	brittle, rigid, and non-flexible to design
	Electrostatic	80 $\mu$ W/cm <sup>3</sup>	limited applicability, outputs less energy than other kinetic harvesters, needs a polarization source
Acoustic	Acoustic harvester	1 mW/mm <sup>2</sup>	medium-specific efficiency; highly sensitive to diffraction, attenuation, and reflection losses; generates heat
Biomass	Microbial fuel cells	3.5 mW/cm <sup>2</sup>	challenging design
Ambient RF	Rectenna	1 $\mu$ W/cm <sup>2</sup>	too low energy density

not only increases the total harvested energy but also the opportunities of harvesting from different ambient RF energy sources.

Table 1 compares different EH sources. Notice that the numerical values depend on particular implementations and are just presented for the sake of comparison.

Finally, multiple-source EH systems in a single device can overcome the unpredictability of energy arrival. This technique increases the chance of harvesting at least from one of the sources but at the cost of increasing form factor and the hardware complexity of the circuits and power management unit [37].

### 1.3 Electromagnetic-based WET

The energy arrival from ambient EH sources per time unit depends on the particular source and its availability. This may cause an excessive accumulation of data packets in the sensors' queues until enough energy is available for transmission. Additionally, EH from ambient RF transmissions restricts the deployment of IoT networks in rural areas, where the network infrastructure is scarce or nonexistent, and its applicability is limited to ultra-low power consumption devices. Hence, powering the variety of coming IoT applications with only these solutions makes difficult to meet stringent QoS requirements (e.g., low delay, moderate to high data rate, high reliability, etc).

Meanwhile, electromagnetic-based WET constitutes a promising technology for wirelessly charging next-generation devices. It can be classified into near-field (nonradiative region) and far-field (radiative region) techniques. Near-field techniques have already gained popularity in the electronic industry, for charging mobile phones, tablets, smartwatches, and other electronic appliances [28]. As an example, the inductive coupling technology transfers energy between coils throughout magnetic fields just as

in the conventional AC transformers. The transmission occurs within the range of a few centimetres, and with better efficiency as the frequency increases. Usually, both transmitter and receiver coils are designed with different resonant frequencies. The main problem with inductive coupling is that the alignment of the coils highly conditions the amount of received energy. On the other hand, a magnetic resonator transfers energy using high-quality resonant circuits tuned at the same frequency. Although this technique achieves lower efficiencies in short distances compared with its inductive coupling counterpart, it does extend the transmission range to tens of centimetres.

On the other hand, far-field WET technologies allow overcoming larger distances using laser power beaming or microwave-based WET. Laser power beaming technology transfers energy by steering laser beams towards specialized photovoltaic cells over long distances. However, laser-based WET works on LoS links with precise alignment between transmitter and receiver; and its efficiency hinge on the atmospheric absorption and scattering by clouds, fog, and rain [38]. Besides, laser radiation causes harm even at low-power applications either by pointing directly the beam or by reflections.

Meanwhile, microwave-based WET or simply RF-WET relies on energy transmitters called power beacons (PBs) that radiate microwave signals to power the devices. RF-WET is considered a potential enabler for wirelessly charging massive IoT deployments [3]. The three canonical network models for RF-WET are: i) pure WET, ii) wireless powered communication network (WPCN), and iii) simultaneous wireless information and power transfer (SWIPT). In the first case, the energy transmitter sustains the devices' operation without exchanging any data. In WPCN, the sensors harvest energy from downlink transmissions from the energy transmitter(s) and then use it to upload sensing information to an information AP. Finally, SWIPT aims to efficiently use the spectrum resources by embedding both information and energy in the same waveform.

RF-WET is subject to channel impairments such as distant-dependent loss, shadowing and multipath fading, since they convey RF signals. Besides, international telecommunication organizations regulate the maximum transmit power to avoid interference with existing networks or to not cause any harm to human health. These facts, together with the relative low sensitivity of the energy receivers, limit considerably the operating range of RF-WET. Herein, we present some of the state-of-the-art techniques for making RF-WET a viable solution wirelessly powering many the coming IoT use cases.

## 1.4 Thesis contribution

This thesis targets the deployment optimization of PBs for powering a massive IoT network subject to a probabilistic energy outage requirement. Our main contributions are:

- i) we present WET-enabled network models and some RF-WET techniques for powering the coming IoT use cases;
- ii) we discuss the role of EH from ambient sources to sustain IoT networks;
- iii) we discuss some health concerns about RF-WET and the magnitudes for characterizing the impact of the RF radiation on human beings;

- iv) we propose an algorithm for minimizing the number of PBs required to meet a network-wide energy QoS requirement;
- v) we evaluate several methods for optimizing the PBs' positions to power a massive number of IoT sensors;
- vi) based on our analytical approximations, we find that in a scenario with up to two PBs, the optimal strategy is to place a single PB at the circle center with radius  $R$ , assuming the same total power. Meanwhile, in case of three and four PBs, they should be deployed on a concentric circumference approximately of radius  $\frac{R}{2}$  and  $\frac{R\sqrt{2}}{2}$ , respectively, for optimum performance. For the rest of the cases, the optimal positions depend strictly on  $R$  and the path loss exponent;
- vii) numerical results show that the number of PBs deployed improves more the minimum incident RF power than the number of antennas per PB, even though both help to overcome the energy outage.

## 1.5 Thesis outline

The remainder of the thesis is organized as follows. In Chapter 2, we present a review of the state-of-the-art techniques for implementing RF-WET, as well as typical WET-enabled network architectures. In Chapter 3, we introduce the system model and propose an algorithm for finding the optimal PBs' positions, and compare it with other benchmark strategies. In Chapter 4, we present numerical examples on the optimal deployment of PBs, and some insights on the impact of multi-antenna PBs-assisted WET and the maximum coverage area. Finally, Chapter 5 concludes the thesis.

## 2 RF WIRELESS ENERGY TRANSFER

In contrast to EH from ambient energy sources, RF-EH from dedicated PBs provides a predictable energy source for wirelessly powering the network with minimum impact to current IoT devices' design. The operation range of RF-WET depends on the antenna gains, transmit power, operating frequency, channel conditions and receiver sensitivity, and extends over much larger distances compared to its near-field technology counterparts. Besides, RF-WET promises support to scenarios with non-LoS (NLoS) conditions, energy broadcast to power multiple devices simultaneously, and mobile users. Table 2 compares RF-WET with other electromagnetic-based WET technologies. Hereafter, we use WET to refer exclusively to RF-based WET.

Figure 1 depicts a block diagram of an EH receiver. The rectenna is the core module for RF EH since it rectifies the microwave signals to power the IoT devices' circuits or to recharge their battery remotely. The rectenna components are:

- i) receive antenna(s), whose design is optimized for the operating frequency range of the RF energy source. Note that in ambient RF-EH scenarios, the RF energy density varies significantly with frequency, thus receive antennas are typically designed for broadband/multi-band operation instead of a single frequency [3];
- ii) the matching network, which guarantees impedance matching at the designed frequency, and hence maximum power transfer from the antenna to the rectifier circuit. Besides, it prevents energy reflection from the rectifier to the environment, which would reduce the available power for rectification. Matching networks can be implemented with Pi, T, or L sections of reactive lumped components or transmission lines depending on the operating frequency. To obtain a broadband/multi-band matching network, we can connect in cascade/parallel many of these sections, but in practice the loss increases with the number of components [39]. Alternatively, in [40] the authors proposed an impedance-tunable microstrip antenna to match with the input impedance of the rectifier circuit to get rid of the complex impedance matching network;
- iii) the rectifying circuit, which converts the received RF signal into the needed DC voltage to sustain the operation of most of the functional blocks in IoT sensors. A typical choice for rectifying devices are the Schottky diodes due to their low forward voltage drop, low power consumption and very high switching speed [41]. However, since the output of the rectifying circuit is quite low to drive a device directly, it is common the use of a DC-DC multiplier to boost the DC voltage level;
- iv) low-pass filter, which aims to provide a ripple-free signal to charge the energy storage element that can be a conventional battery or a supercapacitor.

Different from EH systems relying on ambient energy sources, WET-enabled networks allow the optimization of the end-to-end efficiency. The end-to-end efficiency of a WET system comprises three components:

- i) DC-RF conversion efficiency at the PB. The power amplifier architecture (i.e. class A, B, C, etc.) at the PB determines the DC-RF conversion efficiency. Although power amplifiers are non-linear devices they can operate in the linear region but it entails high power dissipation at active devices and low conversion efficiency.

Table 2. Comparison among WET technologies [38]

WET Technology	Operating frequency	Main transducer	Characteristics
Inductive coupling	tens Hz - hundreds MHz	wire coil	very high efficiency over units, of cm, relatively small form-factor, highly sensitive to tx/rx misalignment.
Magnetic resonant coupling	hundreds kHz - tens GHz	tuned wired coil	high efficiency over tens of cm, large form-factor, multi-user support.
Laser power beaming	hundreds THz	laser and photoreceiver	high energy delivery up to km, laser radiation can damage biological tissues, sensitive to LoS blockage and atmospheric conditions
RF-WET	hundreds MHz - hundreds GHz	rectenna	low efficiencies over tens of m, very small form-factor, support mobile users, potential NLoS support.

- ii) RF-RF transmission efficiency, which is a function of the channel conditions and improves with highly directional antennas and energy beamforming, which focus sharp energy beams towards the IoT devices. These strategies increase the incident power thus, mitigating the degenerative path loss, and avoiding energy transmissions toward device-free spatial directions. The antenna polarization also plays a role improving the RF-RF efficiency. Circular polarization reduces the mismatch losses caused by other forms of polarization, thus is usually preferred for WET [42].
- iii) RF-DC conversion efficiency at the EH receiver, that depends on the rectifying device, the rectifier topology, and the output load. Besides, the design of the receiver antenna and rectifier circuit must be optimized to the operating frequency for EH. Among the rectifier architectures, the ones with the minimum number of rectifying devices exhibit the best RF-DC conversion efficiency in low-power scenarios, along with a simpler circuit layout [43]. In [43], the authors proposed a method based on harmonic balance simulation subject to a minimum RF-DC conversion efficiency to optimize the rectenna design.

Energy waveform optimization requires a closer look at the transfer function of the EH receiver. The output current of a rectifier circuit is a non-linear function of the input RF power; however, for sufficiently low power levels it can be approximated with a linear function. In such a case, concentrating all the power on a single frequency would suffice as the optimum transmit waveform [44]. This model has been widely applied in many scientific papers provided its mathematical simplicity, e.g., [45–48]. As the input RF power increases, the waveform spectrum impacts more the RF-DC conversion efficiency since the non-linearity dominates in the circuit behaviour. The authors in [38] demonstrated that under the non-linear model, the optimum waveform



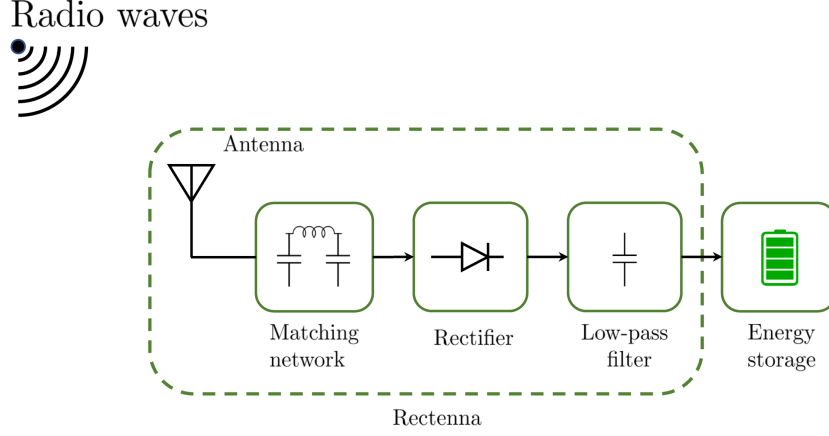


Figure 1. Block diagram of a rectenna.

Table 3. Operational features of some state-of-the-art rectenna modules.

Reference	$\xi_0$ (dBm)	$\xi_{\text{sat}}$ (dBm)	$\eta_{\text{max}}$ (%)	Frequency
[49]	-10	20	50	5.8 GHz
[50]	-15	15	89	915 MHz
[51]	-15	15	90.6	915 MHz
[52]	-20	10	60	1.7 ~ 2.7 GHz
[53]	-20	15	72.8	2.4 GHz
[54]	-10	20	63.38(65.4)	2.4(5.2) GHz

strategy points to allocating the transmit power over multiple sinewaves, whose additional contribution scales up linearly with the number of tones in flat fading channels. Moreover, in frequency-selective channels, the optimum waveform allocates more power to the frequencies with the higher channel gains.

In general, the non-linear model of the EH circuit distinguishes three regions:

- i) zero-output power, in which the input RF power level is below the sensitivity of the circuit;
- ii) input power-dependent region, where the output DC power is a non-linear function of the input RF power level;
- iii) saturation region, where the output DC power becomes nearly constant and independent of the input RF level.

Table 3 lists typical values the sensitivity ( $\xi_0$ ) and saturation ( $\xi_{\text{sat}}$ ) levels, maximum RF-DC conversion efficiency ( $\eta_{\text{max}}$ ) and operating frequency of some state-of-the-art rectennas.

To capture this non-linearity in a mathematical model, in [55], the authors proposed the sigmoid function to describe the transfer characteristic of the EH circuit as

$$f(\xi^{\text{RF}}) = \frac{\frac{\xi_{\text{max}}}{1 - e^{-c_1(\xi^{\text{RF}} - c_2)}} - \xi_{\text{max}}\Omega}{1 - \Omega}, \quad (1)$$

where  $\xi_{\max}$  is the maximum output power,  $\Omega = \frac{1}{1+e^{c_1 c_2}}$  is a constant to guarantee zero-input/zero-output response, and the constants  $c_1$  and  $c_2$  are obtained from standard curve fitting. In [56], a rational transfer function is obtained by standard curve fitting considering the dependence of the RF-DC efficiency on the input power. Under this model, the harvested power is

$$f(\xi^{\text{RF}}) = \frac{c_1 \xi^{\text{RF}} + c_2}{\xi^{\text{RF}} + c_3} - \frac{c_2}{c_3}, \quad (2)$$

which has zero-input/zero-output response, and  $f(\xi^{\text{RF}}) \rightarrow c_1 - \frac{c_2}{c_3}$  as  $\xi^{\text{RF}} \rightarrow +\infty$ . However, increasing the accuracy of the EH circuit's model also makes the analysis more intricate, even in a very simple scenario. A simpler, but yet effective, approach assumes that the input power-dependent region follows a linear function while considering the sensitivity and saturation phenomena [57]-[58]. The input-output relationship in this case is modelled with a piecewise function as

$$f(\xi^{\text{RF}}) = \begin{cases} 0, & \xi^{\text{RF}} < \xi_0, \\ \eta \xi^{\text{RF}}, & \xi_0 \leq \xi^{\text{RF}} < \xi_{\text{sat}}, \\ \eta \xi_{\text{sat}}, & \xi^{\text{RF}} \geq \xi_{\text{sat}}. \end{cases} \quad (3)$$

Similarly, in [59] the non-linear region is approximated with a series of line segments which improves the modeling accuracy but increases the complexity as it includes more segments.

## 2.1 Multi-antenna WET scenarios

The integration of the energy receiver into the existing IoT hardware follows two main trends. On one hand, rectennas can share the same antennas with the existing information decoding (ID) circuits, which implies that the design must undergo significant hardware modifications. Indeed, sharing the same antennas entails the use of an additional block that switches between ID and EH, and requires the use of the same frequency band for both receivers. On the other hand, the implementation of independent energy receivers with dedicated antennas eases its integration into the existing designs, and allows independent and concurrent operations.

In case of scenarios with multi-antenna energy receivers, one may need to figure out what is more appropriate: combining the DC signal coming after the rectification process or combining the received signal at the RF stage [60]. As an example, Figure 2 illustrates these cases in a multiple-input and multiple-output (MIMO) point-to-point WET scenario. In the former strategy, as Figure 2a depicts, each antenna feeds a single energy rectifier and the output results as the combination of individual DC signals. In the latter, a frequency-dependent analogue combiner drives the input of the energy rectifier; thus, improving the RF-DC efficiency since now it can operate in high RF power input regime (Figure 2b). Although both strategies boost the output power as the number of antennas increases, the RF combining method exhibits the best performance by far. However, and besides the passive RF combiners design challenges, both transmit and receive ends require accurate CSI for jointly optimizing transmit beamforming and RF combining, in contrast with DC combining that only requires CSI at the PB. Multi-antenna energy receivers come with another advantage: they could ease the design of EH

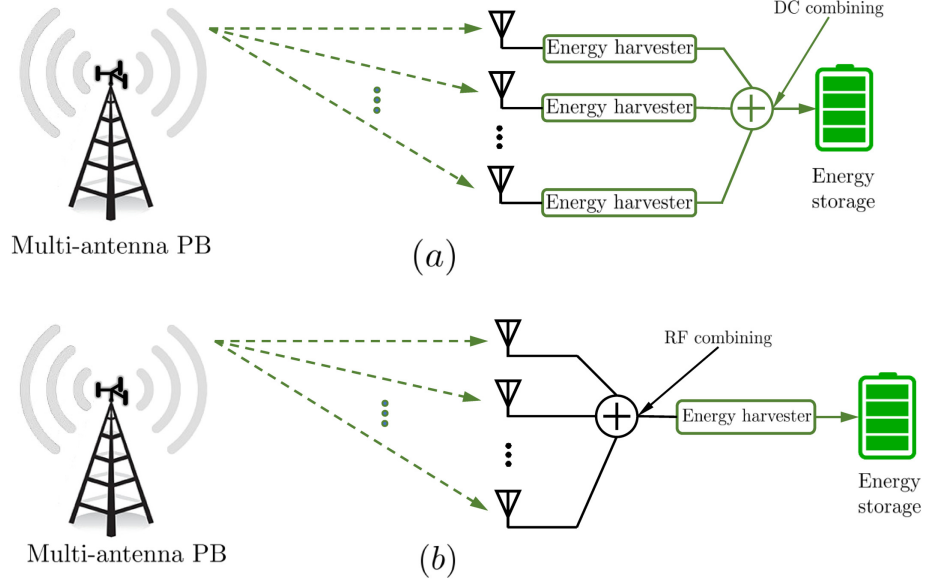


Figure 2. Examples of WET receiver architectures in a MIMO point-to-point scenario: a) DC combining; b) RF combining.

circuits with a broad dynamic range. Instead of designing a complex rectenna, we can use multiple rectifiers with different sensitivity and saturation levels that optimize the connection to the receive antennas according to the incident RF power [61].

WET implementations also distinguish from architectures with co-located and distributed antennas (DAS) at the PBs; while co-located antennas perform energy beamforming to extend the WET range, the DAS strategy can overcome the effects of the large-scale fading. In [62], the authors compared two WPCN setups: one served by a PB equipped with a uniform linear array, and other with distributed single antenna PBs. They showed that devices under the former deployment strategy achieve higher incident power levels when maximizing the minimum incident RF power, but most of the service area remains energy-silent. On the contrary, the distributed system powers uniformly the service area with higher minimum power levels due to the reduced distance between PBs and sensors.

### 2.1.1 On the CSI estimation for WET

Different from conventional wireless communications, in WET scenarios the energy receiver doesn't require CSI for proper operation in general. However, optimal energy beamforming and waveform power allocation under frequency-selective channels require accurate CSI at the transmitter. State-of-the-art literature describes three algorithms for estimating the CSI for WET purposes [62]:

- i) forward-link training with CSI feedback, where the PB sends pilots to the IoT devices, which after performing the computation feedback the estimated CSI to the PB using a different channel (Figure 3.a). The main problem with this strategy is that the training overhead scales up with the number of antennas which requires extra processing from the low-cost device;

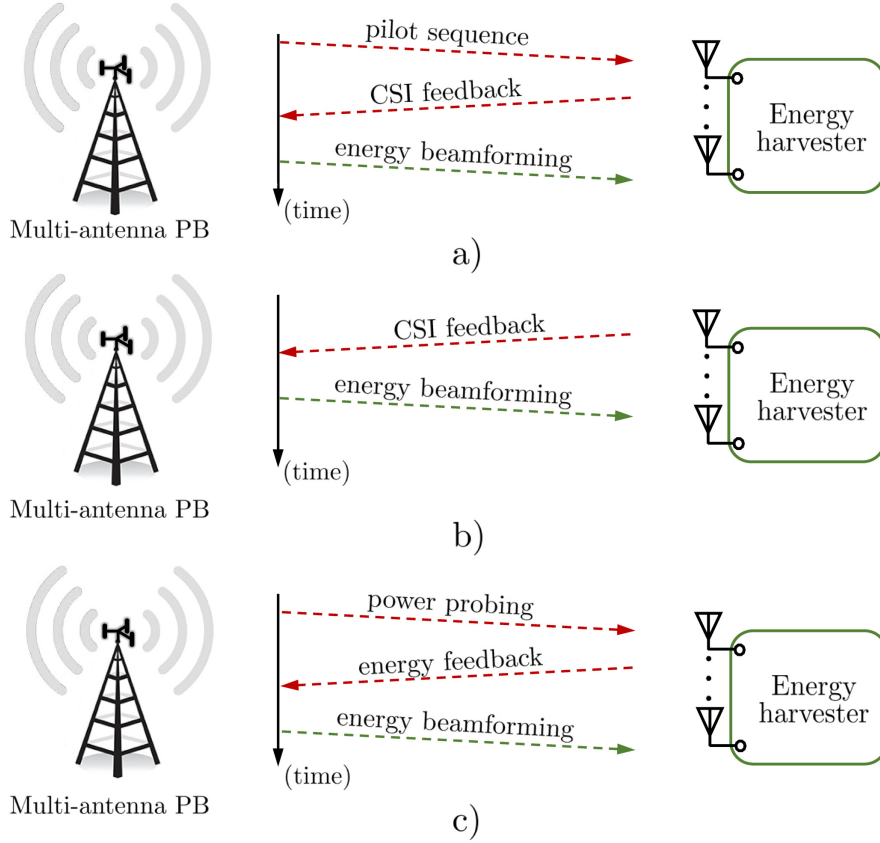


Figure 3. Algorithms for estimating the CSI: a) forward-link training with CSI feedback; b) reverse-link training; power-probing with energy feedback.

- ii) reverse-link training, the IoT devices send pilots to the PB for further estimation, assuming that channel reciprocity holds (Figure 3.b). This method reduces the processing overhead at the IoT device, and the time/energy consumption is independent of the number of antennas;
- iii) power-probing with energy feedback. While the previous algorithms apply only for the shared-antennas architecture, the power-probing with energy feedback is suitable for the separated-antennas architecture. As Figure 3.c depicts, the PB sends energy probing signals and the IoT device feedbacks the amount of harvested energy during each interval. This technique reduces the processing overhead at the IoT devices and keeps running the EH. However, the complexity of this algorithm also increases with the number of antennas.

## 2.2 Wireless powered communication networks

WPCNs represent a self-sustainable paradigm within traditional wireless sensor networks by using WET-enabled technologies for extending the lifetime of the sensors. WPCNs are environmental-friendly in the sense of reducing frequent battery replacements which generate chemical waste. In a WPCN, WET using dedicated resources, e.g., time,

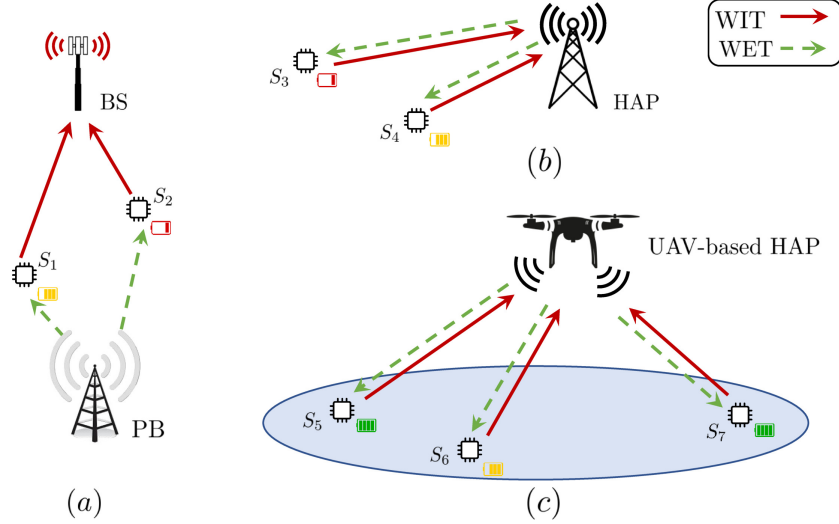


Figure 4. WPCN scenarios: a) separated information and energy transmitters; b) terrestrial HAP-assisted WPCN ; c) flying HAP-assisted WPCN.

frequency, occurs in the downlink while the wireless information transfer (WIT) happens in the uplink. Figure 4 depicts some WPCN scenarios.

In Figure 4a, a PB powers  $S_1$  and  $S_2$  devices, which then aim to upload their data to a traditional BS, exemplifying the integration of WET into the current wireless infrastructure. Although this model corresponds to a separated implementation of both information and energy transmitters, these functionalities can be combined into a hybrid AP (HAP) as Figure 4b and Figure 4c depict. Compared with the separated implementation, a HAP facilitates the coordination between information and energy transmissions and reduces the costs provided that both functions share common hardware.

In practice, the difference between information and energy sensitivity at an IoT device challenges the implementation of WPCN. While traditional ID circuits can operate with an input power usually greater than  $-60$  dBm, state-of-the-art rectennas requires at least  $-10$  dBm, thus making the range for WET and WIT quite different. Hence, a HAP-enabled WPCN raises the so-called doubly-near-far problem, where the most distant sensors harvest less energy but require more energy for uplink transmissions. For instance,  $S_3$  is most likely to empty first its battery compared with  $S_4$  which is located nearest to the HAP in Figure 4b. This unfair condition questions the combination of WET and WIT in a single AP.

Nevertheless, the use of an unmanned aerial vehicle (UAV) as a HAP in Figure 4c can eliminate the doubly-near-far problem. UAVs are attractive candidates in WPCN as they can act as a flying BS in places without telecommunication infrastructure or where is too risky for human intervention. The 3D mobility of the UAVs also helps to avoid obstacles, improves WET efficiency, and reduces the installation/operational costs in large areas. Typical applications range from smart agriculture [63], water monitoring, smart cities, etc. Despite the flexibility of a UAV-based HAP, yet there are challenges associated with 3D optimal trajectory planning, energy-efficient UAVs' designs, strong air-to-ground interference due to the high-probability LoS channels, and the need for lightweight and compact communication hardware design [64].

Dynamic allocation of time-frequency resources for WET/WIT rounds can help to mitigate the doubly-near-far problem. Based on the CSI, battery state, and communication demands, the network can adaptively schedule more time slots for WET/WIT or allocate the best frequency channels for WET to serve the far-away devices. However, in scenarios with high mobility, where the channel conditions vary rapidly with time, dynamic resource allocation can be very challenging. On the other hand, in the spatial domain, the PBs and BSs can prioritize some devices by performing energy and information beamforming. Besides, multi-antenna technology allows the BSs to decode packets that arrive simultaneously from the sensors, which boosts the network throughput over multiple time-frequency blocks.

### 2.2.1 Cooperative WPCNs

Cooperation also alleviates the degradation caused by the doubly-near-far problem. The IoT sensors closer to the HAP can relay the information of the far-away sensors, in addition to broadcast to them part of its harvested energy [65]. A typical cooperative strategy includes three phases: in the first time slot, the HAP performs WET to power the network; during the second time slot, the far-away sensors transmit its data to the relay sensor; and finally, the relay forwards all the information to the HAP. The relay sensor can either amplify-and-forward (AF) the incoming packets or decode-and-forward (DF) them to the HAP. While AF is simpler and faster, the DF protocol invests time and computational resources in decoding the incoming information, while it jointly encodes it with the relay's data to reduce the time-on-air. An interesting scenario consisting of a relay-assisted WPCN that operates in full-duplex mode is studied in [66]. The benefits of a full-duplex-enabled relay are two-fold: i) it ensures concurrent WIT and EH at the relay; and ii) it enables an energy-efficient solution called self-energy recycling since the relay also harvests energy from self-transmissions in the WIT rounds. Significant throughput improvements are attainable compared to the conventional time-switching based relay strategy. In [67], the authors used geodesic geometry to design a joint downlink-uplink beamforming strategy in a MIMO relay-assisted network. They developed an uplink/downlink protocol for the MIMO relay channel that consists in four stages: i) first, an AP sends data to the relay; ii) during the second period, the relay forward the data to the end-user, and simultaneously performs EH and self-energy recycling; iii) in the third slot, the end-user uploads data to the relay; and finally iv) the relay forwards the end-user data to the AP while performing EH and self-energy recycling from it. Self-energy recycling potentially reduces the energy drawn from the power grid to the BSs. In [68], the authors maximized the energy efficiency at the BS, defined as the ratio of the throughput and the energy consumption from the power grid, that serves one downlink and one uplink single-antenna device. They demonstrated the benefit of self-energy recycling vanishes for high uplink traffic since the BS must turn on the self-interference cancellation circuit most of the time.

### 2.2.2 Power control protocols in WPCNs

At this point, the reader may be wondering how WPCNs schedule WET/WIT rounds. To begin with, a harvest-then-transmit protocol (HTT) allows wireless devices to first harvest sufficient energy before initiating information transmissions [69]. It assumes no energy accumulation between transmission rounds; hence, devices can perform WIT exhausting all the power available in their batteries or supercapacitors. In multi-user WPCNs, the protocol allocates WIT timeslots for each user according to the target data rate. The HTT protocol's schedule for WIT/WET has an impact in the trade-off between the amount of harvestable energy and the achievable data rate, which defines the rate-energy region. On one hand, if the WET phase is too short (or the channel behaves poorly during WET), the transmit power decreases affecting the receive SNR, and thus the achievable rate. On the other hand, if the network schedules short periods for WIT, the transmission time decreases, which also affects the rate. The fixed threshold transmission (FTT) protocol proposed in [70] allows the sensors to transmit their data as long as the required power is below a predefined threshold, otherwise, they save the energy for future transmissions. However, the authors of [70] assumed large block lengths and battery capacity. In an attempt to fill this gap, the authors of [71] proposed alternative strategies namely finite block-FTT (FB-FTT) and finite blocklength fixed threshold uninterrupted transmission (FB-FTUT). In the former, the sensors target an error probability and only transmit if the energy available in the battery is sufficient, otherwise they save it for the next round. On the other hand, the FB-FTUT protocol allows transmitting with maximum power when it is not possible to achieve the target probability of error. Both strategies outperform the benchmark scenario using the HTT protocol, which highlights the significance of energy accumulation between transmission rounds.

### 2.2.3 Ambient EH-assisted WPCNs

EH from ambient sources can be a fundamental component in WPCN. Indeed, the IoT sensors can harvest energy from renewable energy sources and RF transmitters, in addition to the pre-scheduled downlink WET rounds. In [45], the authors determined an activation rule for WET to maximize the weighted sum-rate of the network. Based on the battery state at the beginning of the transmission block, the hardware specifications of the sensors and the CSI, the HAP estimates if the sensor's battery suffices for successful WIT. Moreover, numerical experiments show that as the distance from the HAP increases, the nodes rely more upon the ambient sources whereas WET is no longer needed. This approach not only improves the throughput and reliability of the WPCN but also saves part of the energy budget at the HAP. This is a desirable outcome in 5G and beyond wireless networks, where the BSs (and probably the HAP/PB) support massive MIMO and convey more traffic than 4G cellular networks. Currently, the telecommunication sector stands for approximately 7% of the total global electricity; but, by 2030 this contribution will represent a 51% with a carbon footprint of 23% provided the network densification [72]. For that reason, EH at the BSs will alleviate the carbon emission since BSs account for most of the energy consumption of the wireless networks. As an example, EH at a HAP has been considered in [73], where the authors jointly optimized WET/WIT to maximize the network sum-rate considering the energy arrival rate. Different from

IoT sensors, BSs are bigger and more complex; hence, they could integrate bigger solar panels or eolic turbines, which increases the harvested energy. Meanwhile, PBs/HAPs can properly control the power and/or use beamforming to wirelessly power the sensors that are harvesting insufficient renewable energy.

### 2.3 Simultaneous wireless information and power transfer

Within WET-enabled networks, SWIPT opens up new opportunities as it targets WIT and WET simultaneously using the same channel resources. The main challenge in SWIPT is given by the different nature of WET/WIT. While high to moderate SNR values suffices for ID, the energy receiver, on the other hand, requires significant incident power. SWIPT implementations expand through different domains such as time, power, antenna, and space as shown in Figure 5 [74], [75]. The time switching (TS) technique divides the time for WET and WIT (Figure 5a). In this way, the transmitter could perform separated energy and information beamforming (or other transmission or resource allocation strategies) at each corresponding time. Although TS receiver implementations are simple they require accurate time synchronization. The parameter  $\alpha$  establishes how information and energy are scheduled; but, depending on the battery state of the IoT sensor, the system could dynamically adjust energy/information rounds to optimize the performance. As Figure 5b shows, the power splitting (PS) architecture divides the power of the received signal between EH and ID. Different from TS, PS strictly does achieve SWIPT, at the cost of the high complexity of the PS circuit, since the received signal is used for both ID and EH. Hence, PS is suitable for time-critical applications with information/energy or delay constraints and performs close to the information theoretical optimum. By varying the splitting ratio  $\rho$ , the system achieves different points in the energy-rate region. A more general model, the so-called dynamic power splitting (DPS), is described in [76]. Here, the power splitting ratio changes over time according to the CSI, and the ID circuit alternates between on-off periods to save battery. The reader can notice that TS and PS are special cases of this model. If the power splitting ratio takes on 0 or 1 within the transmission interval it operates in TS mode. In PS mode, the ID remains on and the power splitting ratio is fixed over time. Finally, in on-off mode, the first symbols are dedicated to EH, and for the remaining time, the circuit splits the power between ID and EH. On the other hand, the antenna switching (AS) architecture performs SWIPT in the antenna domain by grouping the receive antennas for ID and EH (Figure 5c). For a particular channel realization, the system computes the optimum antenna assignment for each receiver. The main issue with AS is that the computational complexity increases exponentially with the number of antennas. The authors in [77] proposed a polynomial-time complexity algorithm by transforming a single-input multiple-output (SIMO) channel into an equivalent single-input single-output (SISO) with a single virtual antenna. Numerical results in this work show that the sub-optimal strategy approaches the optimum SIMO PS results for a large number of antennas. In [78], the authors proposed a low-complexity AS strategy for a MIMO relay channel using generalized selection combining circuits at the input of the ID and the energy harvester. The best antenna channels are assigned dynamically according to the QoS requirements and the fading state. Finally, SWIPT can also exploit the degrees of freedom of the MIMO channel in the spatial domain as Figure 5d depicts.



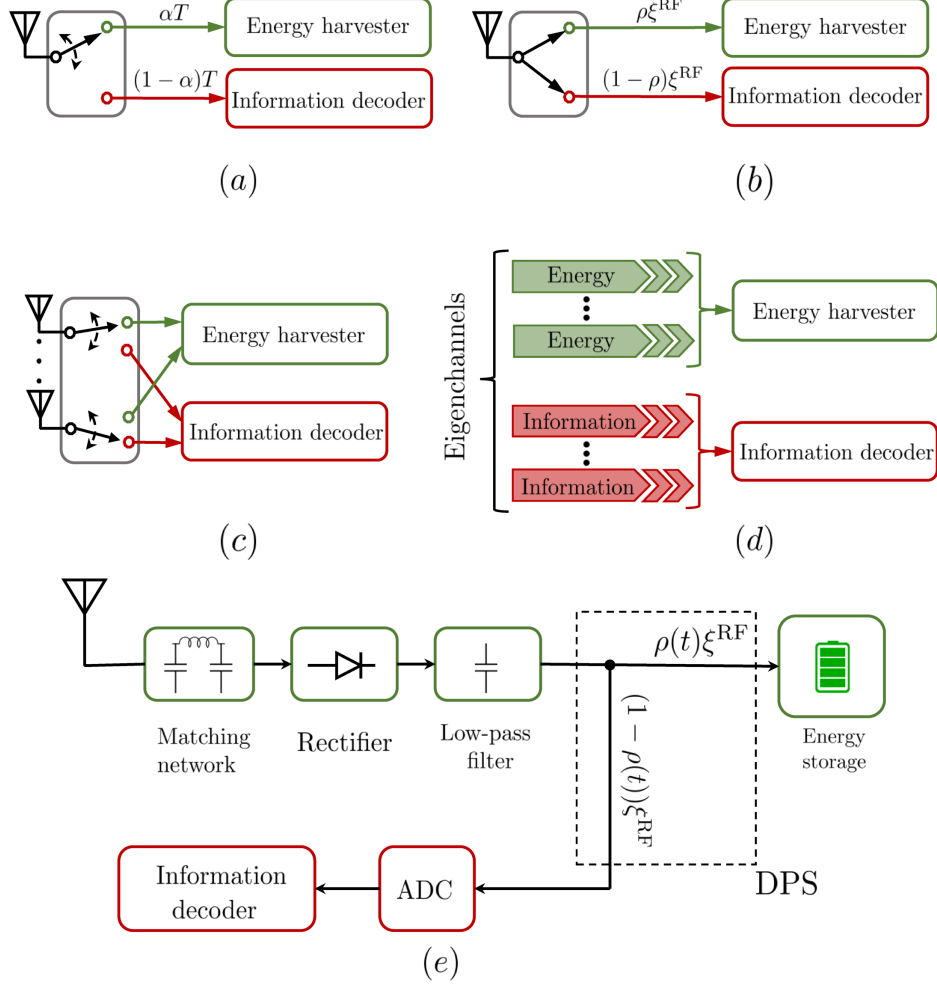


Figure 5. SWIPT receiver architectures examples: a) time switching; b) power splitting; c) antenna switching; d) space switching; e) integrated receiver.

Indeed, the singular value decomposition shows that the MIMO channel matrix contains independent streams or eigenchannels that can carry either information or energy. The optimal eigenchannel assignment is a complex combinatorial problem, and the authors in [79] have addressed this problem under limited CSI. They proposed a polynomial-time complexity algorithm that minimizes the sum transmit power while meeting energy and ID constraints.

So far, we have presented architectures with separated energy and ID circuits at the IoT receivers. However, the traditional RF chain of the ID circuits consumes a significant portion of the energy budget to perform baseband conversion, and decoding the information directly from the energy-carrying signal is yet challenging. This is why the authors in [76] proposed a novel receiver architecture that integrates both ID and EH substituting the conventional baseband converter with the rectifier of the EH circuit (Figure 5e). The advantages of this architecture are three-fold:

- i) reduces the net energy consumption (nearly zero) since eliminates most of the active elements;
- ii) allows continuous WIT without degrading the WET efficiency;

- iii) delivers high SNR signal at the input of the ID at moderate distances.

Moreover, the authors proposed a new energy modulation scheme where the information signal modulates the amplitude of the energy-carrying signal. Numerical results evidence that this proposal achieves better energy-rate performance compared to the separated architecture within moderate distances. Beyond a certain point, the separated architecture with DPS outperforms such implementation.

In general, accurate CSI at the transmitter (CSIT) helps to improve the achievable rate-energy performance at the receiver for both DPS and TS schemes. Moreover, as compared to TS, DPS achieves substantially improved rate-energy trade-offs towards the performance upper bound. The authors in [77] concluded that:

- i) when CSIT is available and channel condition is poor, the optimal strategy is to terminate the transmission and save energy in both receivers. Meanwhile, in moderate fading states, the transmitter performs water filling and the IoT sensors allocate all the received power for ID, i.e.,  $\alpha = 0$  for TS and  $\rho(t) = 0$  for DPS. Finally, when the channel is in a good state, the optimal strategy is to transmit with maximum power and: i) dedicate the receive power for the EH circuit in the TS scheme ( $\alpha = 1$ ), or ii) allocate constant amounts of power for both ID and EH in the DPS scheme.
- ii) without CSI and in poor fading conditions, the optimal strategy at both receiver schemes, is to allocate all the resources for ID. Meanwhile, when the channel is in a good state, the TS strategy allocates all the received power for ID while DPS splits the receive power for both ID and EH using a constant PS ratio.

Although interference is a well-known adversary for traditional wireless communications, it can be used wisely to boost the EH in energy receivers [80]. Indeed, the energy receiver cannot distinguish from the information-carrying signal and the actual interference, which opens up the doors for opportunistic EH in spectrum sharing scenarios. A simple rule is stated in [81]: activate the ID in high signal-to-interference-plus-noise ratio (SINR) regime and a weak received signal, otherwise perform EH. Intentional interference/noise can be also beneficial for EH. For instance, one strategy at the physical layer is to add artificial noise, known by the authorized user, to the actual signal, to make difficult the job of the eavesdropper. This strategy not only improves the communication secrecy but also the artificial noise contributes to the EH efficiency.

## 2.4 Health concerns about WET

The use of massive MIMO to narrow the beams, and smaller cells to bring connectivity close to the end-users in 5G and beyond cellular networks, raise concerns about the possible impact of electromagnetic radiation fields (EMF) levels on the human health, especially above 6 GHz where the radiation absorption increases. These concerns extend to WET-enabled technologies, as it also implies the transmission of RF signals. In order to get some insights, we discuss about fundamentals quantities to measure the intensity and effect of the EMF, as the specific absorption rate (SAR) and plane-wave equivalent power density (PD). While PD is the power flux density of a plane wave, SAR measures

the energy absorbed per body mass when exposed to EMF. A study in [82] analyzes the maximum possible exposure that causes downlink 5G beamforming and compares it with previous cellular technologies. The authors highlighted the effectiveness of SAR when describing the impact of wireless communications on humans since it describes more accurately the amount of absorbed energy than PD. Finally, they also showed that SAR in 5G networks can exceed the guidelines provided by the Federal Communications Commission or the International Commission (FCC) (near-field SAR up to 1.6 W/kg) on International Commission on NonIonizing Radiation Protection (ICNIRP) (near-field SAR up to 2 W/kg) when human users are located close to the BSs. In [83], extensive simulations using a layered model of the human skin show a correlation between PD and the peak temperature elevation in tissue. Taking into account such concerns, the authors in [84] proposed a protocol for associating the end-users with the BS such that the latter complies with the PD restriction of maximum 10 W/m<sup>2</sup> (established by the FCC and the ICNIRP). Besides, they studied the effectiveness of the aforementioned metrics when describing the effect of the EMF at high frequencies ( $> 28$  GHz) on human health, where highly directional beams are more usual since WET faces a severe attenuation and penetration loss due to the high frequency. In this direction, the authors in [3] discussed the use of a DAS, together with real-time human presence detection to avoid steering energy towards the human body. Despite all these facts, far more evidence is needed to ensure the potential WET health impact under real-life conditions [85]-[86].

## 2.5 Optimization deployment of energy and information transmitters

The development of algorithms for optimizing the deployment of energy and information transmitters have taken the attention of the research community as they constitute potential enablers towards meeting stringent QoS requirements. For example, the authors in [87] minimized the cost of deploying PBs with directional antennas to guarantee a minimum incident power at the sensors. They proposed an algorithm for placing the PBs assuming that each candidate position has a certain cost associated to installation, maintenance, and energy supply from the power grid. Similarly, in [87] the authors proposed algorithms for minimizing the placing cost of either separated PBs and BSs or HAPs such that the sensors' battery level always exceeds a certain value. Such algorithms divide the network into non-overlapping clusters relying on the CSI and the sensors' positions; hence, under lack of this information, the solutions could be not optimal. In [88], the authors considered directional antennas to optimize the placement of PBs. Therein, they maximized the overall average harvested energy using a piecewise linear EH model. Authors in [89] proposed a method for placing directional PBs to power a sensor network with arbitrary obstacles. They maximized the weighted sum of harvested energy considering that all devices have different hardware properties. Field experiments with TX91501 wireless power transmitters and rechargeable sensor nodes equipped with P2110 energy receiver (both from Powercast<sup>1</sup>) showed the feasibility of the proposal. A Daubechies wavelet-based algorithm is proposed in [90] to minimize the number of PBs that guarantees full coverage. Starting from random positions, the algorithm first places the chargers using Daubechies wavelet, then it moves the redundant chargers to serve the uncovered sensors. In [91], the authors proposed a framework to minimize the number of

---

<sup>1</sup>For more information about Powercast devices visit <https://www.powercastco.com/>.

PBs such that the network meets an area spectrum efficiency requirement, defined as the sum rate per unit bandwidth per unit area, and a minimum harvested energy per sensors. The sensors perform device-to-device information transmissions using millimeter waves (mmWave) channels. The authors in [92] optimized the deployment of directional PBs with limited mobility to maximize the network-wide harvested energy. For powering the network, the algorithm moves and rotates each PBs within a circle during the charging time according to the network conditions. They conducted field experiments to test the proposal performance against benchmark strategies. In [93], the authors proposed an algorithm to maximize the weighted sum harvested energy by scheduling the charging time and the PBs' orientations. The proposed framework computes online the optimum charging strategy assuming that each PB can rotate while remaining in a fixed position. In [94], a non-uniform PB deployment is proposed to charge the sensors in a WPCN served by a HAP. To tackle the doubly-near-far problem, the authors proposed that PBs should assist the far away sensors unreachable by the HAP. Therein, they minimized the total energy consumption subject to a coverage probability threshold and compare it with the case where a BS is used instead of a HAP. In [95], the authors considered the optimal placement of sensors and PBs using the electric field intensity of the WET wave. This framework describes WET technologies from the perspective of constructive/destructive interference of the electric field intensity vectors which seems more accurate for some scenarios. Taking this into consideration, authors of [96] addressed the problem of adjusting the phase shift at each antenna to maximize the overall received power at selected points of the network.

The concerns about the impact of high EMF levels in human health have become part of the strategies for implementing WET techniques. For example, in [97] the authors considered a PB-assisted network that charges wearable devices of mobile users. They proposed a min-max transmission control strategy to ensure safe levels of EMF in the whole network. Similarly, the authors in [98] proposed a framework for optimizing the position and height of a DAS, where each antenna is connected via underground lines to a PB in order to serve a circular area. The authors maximized the average end-to-end efficiency assuming that CSI is unavailable at the PB and constraining the transmit power for safety reasons. The simulations that were carried out showed that the DAS outperforms the co-located antenna strategy in the considered system model. Similarly, in [99] is designed a charge scheduling algorithm that maximizes the overall average harvested energy in an IoT network subject to a probabilistic EMF constraint.

Most of the aforementioned works rely on the knowledge of CSI at the PBs. However, accurate CSI acquisition is costly and its benefits diminish as the number of sensors increases as evidenced by the authors of [57] for a setup where a multi-antenna PB serves a massive sensor deployment. They studied the statistics of the harvested energy under sensitivity and saturation phenomena for CSI-based/CSI-free strategies. Similarly, the performance of CSI-free strategies considering the phase shift among the antenna elements is investigated in [100], and authors compared it with the assumption of independent signals transmitted by each antenna, and the strategy where each transmit antenna owns a time slot for WET (the so-called switching antennas). They concluded that:

- i) sensors that operate near their sensitivity benefit more from the switching antenna strategies, whereas the ones that operate near to the saturation benefit more from all antennas transmitting independent signals;

- ii) when all antennas transmit the same signal the optimal strategy is to shift the signal phase by  $\pi$  radians over consecutive antennas;
- iii) channel correlation under poor LoS conditions is beneficial under the all antennas transmitting the same signal strategy.

Moreover, in [101] authors studied a WPCN served by a HAP that has dedicated sets of antennas for WET and WIT. Therein, they found that the close optimal beamforming strategy is maximum ratio transmission when the incident RF power at the worst sensor is considerably poor compared with other devices. Numerical experiments showed that the benefits of CSI-based schemes vanish rapidly as the energy consumption for estimating the CSI increases. To overcome the cost of relying on instantaneous CSI, the authors in [101] proposed a low-complexity energy beamforming strategy that utilizes only the first-order statistics of the channel. At each iteration, the proposed algorithm solves a system of linear equations whose complexity is independent of the number of antennas. This low-complexity strategy performs close to the full CSI-based ideal scheme under moderate-to-high LoS conditions. Considering that CSI is only available at the receivers, the authors in [102] designed a SWIPT novel strategy using the so-called random beamforming which generates artificial channel fading. According to the channel state, each receiver performs opportunistic ID or EH. The authors showed that even when a single beam is used, the low-complexity algorithm becomes asymptotically optimum in the high incident power regime.

In an attempt to overcome the necessity for accurate CSI, the authors in [103] optimized the position and speed of a mobile PB without knowing the sensors' positions. They assumed that a fence protects the network and the PB can just move in the contour of the service area. The proposed algorithm minimizes the overall charging time while improving the instantaneous minimum incident power, which changes as the PB moves.

In contrast to the aforementioned works, herein, we focus on the optimal deployment of PBs for powering a massive IoT network, in order to satisfy an energy outage QoS requirement. We assume that instantaneous CSI estimation is not practical due to the massive number of sensors, and sensors' positions are unknown at the PBs. Therefore, we optimize the PBs' deployment for maximizing the minimum average RF energy available in the service area, which guarantees for each sensor to most likely meet its corresponding energy outage requirement. Our proposed algorithm is independent of both the hardware heterogeneity and the mobility of the sensors.

### 3 PBS DEPLOYMENT FOR MASSIVE WET

In this chapter, we study the optimal PBs deployment problem for wirelessly charging a massive IoT network. We discuss several techniques for finding the optimal PBs positions, and finally propose an algorithm for this purpose.

#### 3.1 System model

Consider the sensor network in Figure 6 where a set  $\mathcal{B} = \{\text{PB}_b | b = 1, 2, \dots, |\mathcal{B}|\}$  of PBs wirelessly power a massive deployment of IoT sensors denoted by the set  $\mathcal{S} = \{S_s | s = 1, 2, \dots, |\mathcal{S}|\}$ , where  $|\mathcal{B}|$  and  $|\mathcal{S}|$  account for the size of each set respectively. The sensor network lies within a circumference of radius  $R$  and each PB transmits at power level  $P$  using an omnidirectional antenna. We also assumed quasi-static channels with independent and identically distributed (i.i.d) Rician fading with factor  $\kappa$ .

We denote the channel coefficient of the link  $\text{PB}_b \rightarrow S_s$  as  $h_{s,b} \in \mathbb{C}$ , and  $h_{s,b} = \alpha + j\beta$  with independent real and imaginary parts  $\alpha, \beta \sim \mathcal{N}(\sqrt{\frac{\kappa}{2(1+\kappa)}}, \frac{1}{2(1+\kappa)})$ . There is no knowledge about sensors' positions, and PBs are not able to estimate the CSI due to the large number of them. Finally, we denote the energy-carrying signal coming from the  $\text{PB}_b$  as  $x_b$ , and consider that independent signals are transmitted from different PBs. Then, the incident RF power at the  $s^{\text{th}}$  sensor is

$$\begin{aligned} \xi_s^{\text{RF}} &= \mathbb{E}_x \left[ \sum_{b=1}^{|\mathcal{B}|} \varrho_{s,b} h_{s,b} x_b x_b^* h_{s,b}^* \right], \\ &\stackrel{(a)}{=} \sum_{b=1}^{|\mathcal{B}|} \varrho_{s,b} \mathbb{E}_x [|h_{s,b} x_b|^2], \\ &\stackrel{(b)}{=} \sum_{b=1}^{|\mathcal{B}|} \varrho_{s,b} |h_{s,b}|^2 \mathbb{E}_x [|x_b|^2], \\ &\stackrel{(c)}{=} P \sum_{b=1}^{|\mathcal{B}|} \varrho_{s,b} |h_{s,b}|^2, \end{aligned} \tag{4}$$

where  $\varrho_{s,b} = K d_{s,b}^{-\gamma}$  comprises the path loss, which depends on the distance  $d_{s,b}$  of the link  $\text{PB}_b \rightarrow S_s$ , path loss exponent  $\gamma$ , and  $K$ , which accounts for other factors as the carrier frequency and antenna gain [104]. Notice that the statistical independence between the energy carrying-signals  $\{x_b\}$  together with the definition of absolute value for complex numbers allow us to take the step (a). Meanwhile, (b) follows from the fact that the expectation operator only applies to the variables  $\{x_b\}$ . Observe that in step (c),  $\mathbb{E}[|x_b|^2] = P, \forall b \in \mathcal{B}$ , where  $P$  is normalized in the time domain which allows us to indistinctly use the terms energy and power for referring the same quantity. Finally, we consider normalized channel power gain, e.g.,  $\mathbb{E}_h [|h_{s,b}|^2] = 1$ .

For the case of a single PB serving the network, the incident RF power at the  $s^{\text{th}}$  sensor is a scaled non-central chi-squared random variable with non-centrality parameter  $2\kappa$  and 2 degrees of freedom, i.e.,

$$\xi_s^{\text{RF}} \sim \frac{\varrho_{s,b}}{2(1+\kappa)} \chi^2(2, 2\kappa). \tag{5}$$

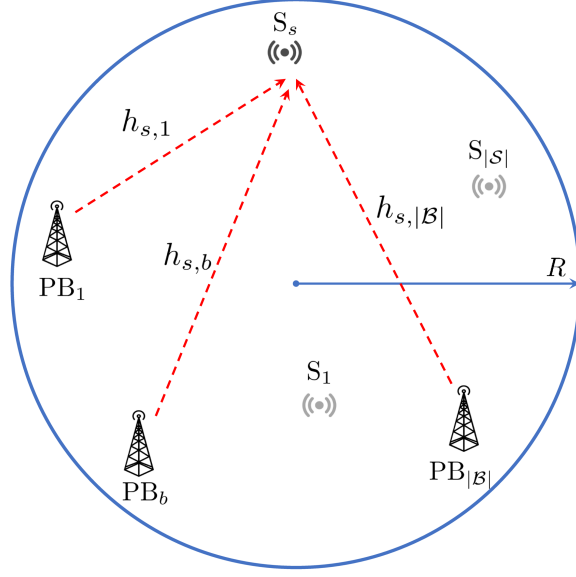


Figure 6. The system model comprises a set of PBs, each equipped with an omnidirectional antenna, deployed to charge wirelessly an IoT sensor network [105].

Hence, when the network comprises  $|B|$  PBs, (5) extends to

$$\xi_s^{\text{RF}} \sim \sum_{b=1}^{|B|} \frac{\varrho_{s,b}}{2(1+\kappa)} \chi^2(2, 2\kappa), \quad (6)$$

which is a linear combination of non-central chi-squared random variables. Herein, (6) follows a generalized chi-square distribution, whose probability density function is often computed by numerical algorithms due to its analytical intractability [106].

### 3.2 Problem formulation

Consider that the PBs charge a massive sensor deployment within a circular service area. Herein, we aim to minimize the number of PBs that need to be deployed in order to satisfy an energy outage probability constraint with threshold  $\zeta$ . Therefore, the ultimate incident RF energy  $\xi_s^{\text{RF}}$  must be above the sensors' sensitivity  $\xi_0$  with probability  $1 - \zeta$ ,  $\forall s \in \mathcal{S}$ . The optimization problem can be formulated as follows

$$\mathbf{P1} : \quad \text{minimize} \quad |B| \quad (7a)$$

$$\text{subject to} \quad \mathbb{P}(\xi_s^{\text{RF}} \leq \xi_0) \leq \zeta, \quad \forall s \in \mathcal{S}, \quad (7b)$$

$$P \leq \frac{P_T}{|B|}. \quad (7c)$$

The reader can notice that  $\mathbf{P1}$  is a mixed-integer programming problem since the objective function  $|B| \in \mathbb{N}$ . In general, the algorithms for solving those problems take non-deterministic polynomial time due to its combinatorial nature [107]. Besides, the constraint (7b) hinders the computation of the outage probability, hence we utilize Monte Carlo simulations when evaluating the distribution of  $\xi_s^{\text{RF}}$ . Finally, the constraint (7c) refers to the per-PB maximum transmit power given the maximum power budget  $P_T$ .

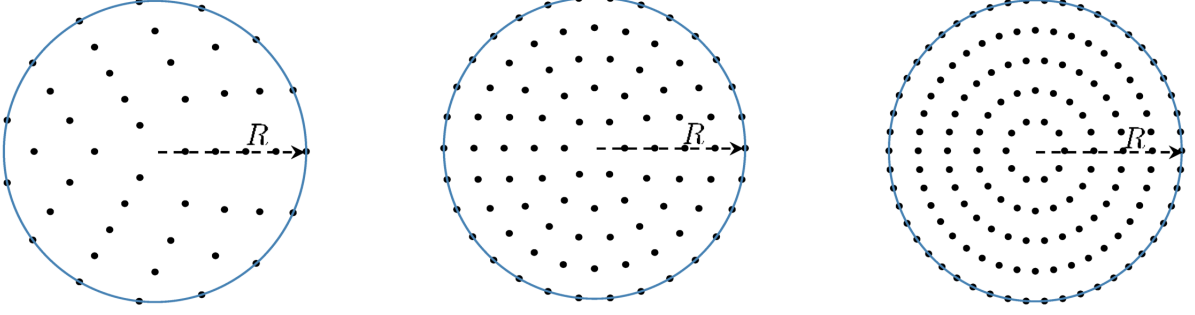


Figure 7. IoT sensor deployments for  $R = 100$  m: i)  $|\mathcal{S}| = 50$  (left); ii)  $|\mathcal{S}| = 100$  (center); iii)  $|\mathcal{S}| = 150$  (right).

### 3.3 On the optimal PBs' positions

For solving the optimization problem **P1** we must count on the optimal positions of PBs given certain channel conditions. Thus, let us fix  $|\mathcal{B}|$  to first find the optimal PBs positions. Without loss of generality, we discretize the circular region where sensors are massively located, hence, mimicking its deployment. As Figure 7 depicts, we create evenly spaced circumferences with a discrete number of points proportional to its radius for mimicking a uniform-like sensor deployment.

The reader can notice that as we increase  $|\mathcal{S}|$ , the points' deployment resembles more the continuous circular area. Let  $\mathbf{u}_s, \mathbf{n}_b \in \mathbb{R}^{2 \times 1}$  denote coordinate vectors for the locations of  $S_s$  and  $PB_b$ , respectively. We can state the average RF energy available at the  $s^{\text{th}}$  sensor, as a function of the distance to each PB as

$$\begin{aligned} \mathbb{E}_h[\xi_s^{\text{RF}}] &= PK \sum_{b=1}^{|\mathcal{B}|} d_{s,b}^{-\gamma}, \\ \mathbb{E}_h[\xi_s^{\text{RF}}] &= PK \sum_{b=1}^{|\mathcal{B}|} \|\mathbf{u}_s - \mathbf{n}_b\|_2^{-\gamma}. \end{aligned} \quad (8)$$

Notice that, in order to meet the system constraints, it is sufficient that the sensor with the minimum incident RF power meets the energy outage requirement. Hence, we can formulate the optimization problem for solving the PBs as

$$\mathbf{P2}: \quad \arg \max_{\{\mathbf{n}_b\}} \quad \min_s \quad \mathbb{E}_h[\xi_s^{\text{RF}}], \quad \forall s \in \mathcal{S}, \quad (9a)$$

$$\text{subject to} \quad \|\mathbf{n}_b\|_2 - R \leq 0, \quad \forall b \in \mathcal{B}, \quad (9b)$$

which maximizes the average received energy at the worst sensor through the optimal deployment of PBs within the coverage area.

#### 3.3.1 Equally-far-from-Center approach (EC)

Considering the radial symmetry of the service area, we first consider a strategy that deploys the PBs equally-far-from the circle center at a distance  $\|\mathbf{n}_b\|_2 = r \leq R, \forall b \in \mathcal{B}$ ,



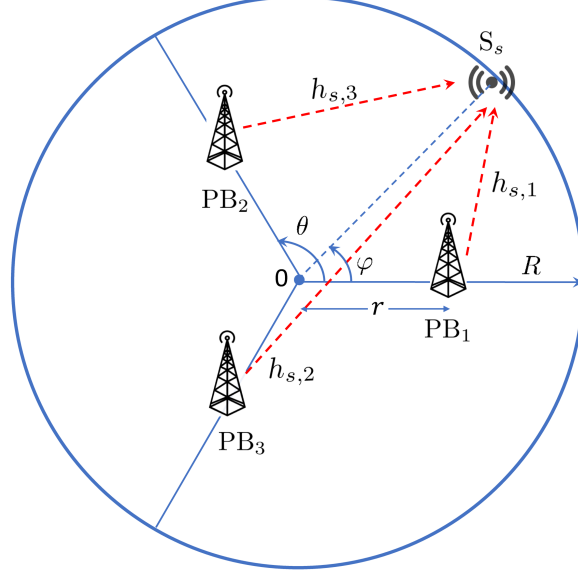


Figure 8. Exemplary deployment of EC for  $|\mathcal{B}| = 3$  [105].

while the angle  $\theta$  determined by any two adjacent PBs and vertex at the circle center must obey

$$\theta = \arccos \frac{\mathbf{n}_b \cdot \mathbf{n}_{b'}}{\|\mathbf{n}_b\|_2 \cdot \|\mathbf{n}_{b'}\|_2} = 2\pi/|\mathcal{B}|, \quad \forall b, b' \in \mathcal{B}, \quad b \neq b'. \quad (10)$$

For this deployment, the worst position in terms of average RF incident power is either at the circumference of the circle or at the circle center, which can be shown using only a small set of PBs and then extend the result for more PBs by symmetry. For the case of  $|\mathcal{B}| = 3$  as depicted in Figure 8, the average incident power at the  $s^{\text{th}}$  sensor on the region's edge using polar coordinates is

$$\mathbb{E}_h[\xi_s^{\text{RF}}] = PK \sum_{b=1}^{|\mathcal{B}|} \left[ r^2 + R^2 - 2rR \cos(\theta(b-1) - \varphi) \right]^{-\frac{\gamma}{2}}, \quad (11)$$

where  $\varphi$  is the angle of the sensor located on the edge. The critical points of (11) are the values of  $\varphi$  within the function domain that satisfy  $\frac{\partial \mathbb{E}_h[\xi_s^{\text{RF}}]}{\partial \varphi} = 0$  or where the derivative doesn't exist. Taking derivatives in (11) gives

$$\frac{\partial \mathbb{E}_h[\xi_s^{\text{RF}}]}{\partial \varphi} = PK \sum_{b=1}^{|\mathcal{B}|} \frac{\gamma r R \sin(\theta(b-1) - \varphi)}{\left[ r^2 + R^2 - 2rR \cos(\theta(b-1) - \varphi) \right]^{\frac{\gamma}{2}}}. \quad (12)$$

For the sake of simplicity, let us neglect the contribution of  $\text{PB}_3$  which is reasonable considering that the signals  $\{x_b\}$  are independent and the superposition principle holds. Hence, we obtain

$$\frac{-\left[ r^2 + R^2 - 2rR \cos(\theta - \varphi) \right]^{\frac{\gamma}{2}+1} \sin \varphi + \left[ r^2 + R^2 - 2rR \cos \varphi \right]^{\frac{\gamma}{2}+1} \sin(\theta - \varphi)}{\left[ r^2 + R^2 - 2rR \cos(\theta - \varphi) \right]^{\frac{\gamma}{2}+1} \left[ r^2 + R^2 - 2rR \cos \varphi \right]^{\frac{\gamma}{2}+1}} = 0, \quad (13)$$

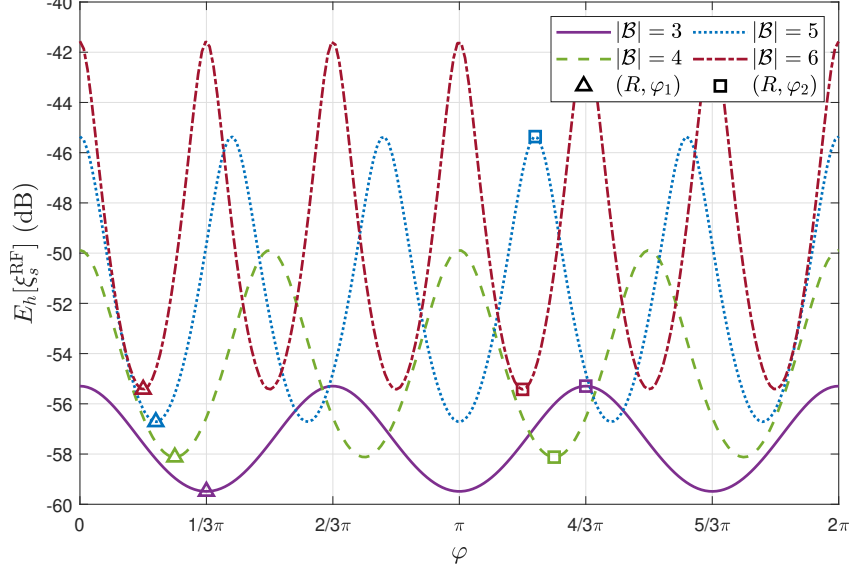


Figure 9. Average incident RF power at the edge vs  $\varphi$  for  $|\mathcal{B}| \in \{3, 4, 5, 6\}$  [105].

which has solution whenever the roots of the numerator exist within the domain of the expression. After reorganizing terms in the numerator we obtain

$$\left[ \frac{r^2 + R^2 - 2rR \cos(\theta - \varphi)}{r^2 + R^2 - 2rR \cos \varphi} \right]^{-\frac{\gamma}{2}-1} = \frac{\sin \varphi}{\sin(\theta + \varphi)}, \quad (14)$$

which has a trivial solution at  $\varphi_{1,2} = \{\theta/2, \theta/2 + \pi\}$  within  $[0, 2\pi]$  when

$$\left[ \frac{r^2 + R^2 - 2rR \cos(\theta - \varphi)}{r^2 + R^2 - 2rR \cos \varphi} \right] = \frac{\sin \varphi}{\sin(\theta + \varphi)} = 1. \quad (15)$$

These solutions correspond to the most distant sensors, equally-far each, from two adjacent PBs. Besides, since  $\mathbb{E}_h[\xi_s^{RF}]$  is a decreasing function of the distance with local maxima at  $(R, 0)$  and  $(R, \theta)$  on the circle edge, the solutions  $\{(R, \varphi_1), (R, \varphi_2)\}$  correspond to local minima. Once we consider the contribution of PB<sub>3</sub>, the point  $(R, \varphi_2)$  receives maximum power possible in the edge, provided it is the closest sensor to PB<sub>3</sub>, while  $(R, \varphi_1)$  remains as a minimum. In the general case  $|\mathcal{B}| \geq 3$ , for  $|\mathcal{B}|$  odd,  $(R, \varphi_2)$  is a local maximum provided the contribution of the PB located at  $(r, \theta/2 + \pi)$ , otherwise is local minimum with the same average received power as  $(R, \varphi_1)$ . Figure 9 depicts the alternate pattern of equally-spaced  $|\mathcal{B}|$  local minima and  $|\mathcal{B}|$  local maxima at the circle edge. Therefore, we adopt  $(R, \varphi_1)$  for finding the value of  $r$  that maximizes the minimum average receive power. Then, let us plug this result into (11) to get the optimum position  $r$  by solving

$$-\frac{2PK(2r - R)}{(r^2 - rR + R^2)^{-\gamma/2-1}} - \frac{PK}{(r + R)^{-\gamma-1}} = 0. \quad (16)$$

The second fractional term in (16) corresponds to the contribution of PB<sub>3</sub>, and can be neglected as the path loss exponent increases, which gives a nearly optimal  $r \approx \frac{R}{2}$ .

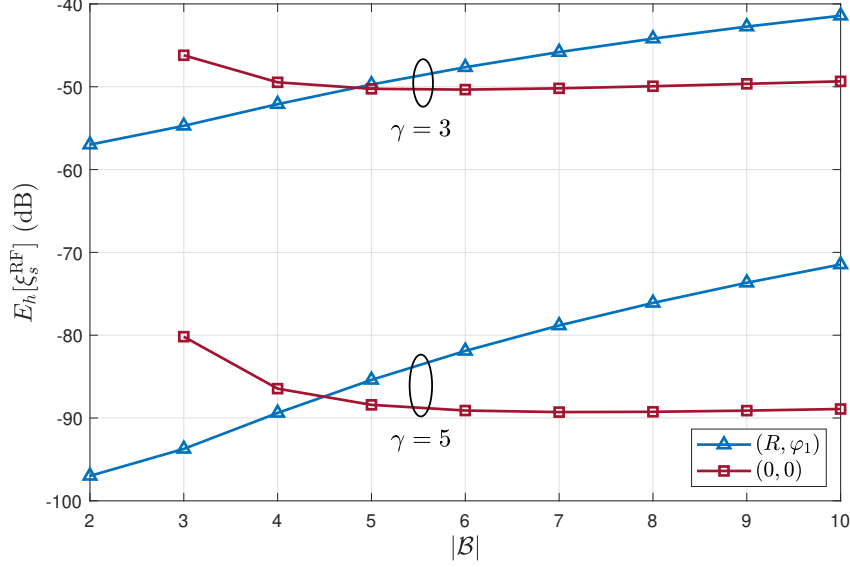


Figure 10. Average incident RF power at both the edge  $(R, \varphi_1)$  and the center vs  $|\mathcal{B}|$  for  $\gamma \in \{3, 5\}$ .

Following the same procedure we can arrive to a general analytical approximation  $r \approx R \cos \frac{\theta}{2}$ , which suggests that for the case of  $|\mathcal{B}| \in \{1, 2\}$ , the placement should be at the center, whereas for  $|\mathcal{B}| = 4$  the placement is  $r \approx \frac{R\sqrt{2}}{2}$  roughly independent of the propagation conditions. It also guarantees that the minimum contribution will be at the circle's edge rather than at the center. For the general case  $|\mathcal{B}| \geq 5$ , the position sensor with the minimum average received power depends on the path loss coefficient  $\varrho_{s,b}$ . For example, Figure 10 depicts the average received power at both the circle center  $(0, 0)$  and  $(R, \varphi_1)$ . Notice that for  $\gamma = 5$  the sensor at  $(0, 0)$  receives the minimum power possible on average. Therefore, this approach doesn't guarantee the best result for an arbitrary  $\mathcal{B}$ , and solving for the case when the optimum kind of deployment is not known a priori is mathematically intractable. Our proposal is to solve the EC approach algorithmically for two topologies: i) as in Figure 8 here called EC; ii) with one PB, the last one, located at the center, thus  $\|\mathbf{n}_{|\mathcal{B}|}\|_2 = 0$ , here called EC with one centered PB. Figure 10 depicts the latter topology where  $\|\mathbf{n}_b\|_2 = r$ ,  $\forall b \in \mathcal{B}$ ,  $b \neq |\mathcal{B}|$ , and the angular separation between them is  $\theta = 2\pi/(|\mathcal{B}| - 1)$ . According to Figure 11, the average received power for the node with  $s^* = \arg \min_s \mathbb{E}_h[\xi_s^{\text{RF}}]$  is

$$\mathbb{E}_h[\xi_{s^*}^{\text{RF}}] = \min \left( \mathbb{E}_h[\xi_{s'}^{\text{RF}}], \mathbb{E}_h[\xi_s^{\text{RF}}] \right), \quad (17)$$

where  $\mathbb{E}_h[\xi_s^{\text{RF}}]$  is the contribution at the worst sensor on the edge with  $\varphi = \varphi_1$ , thus given by (11), and  $\mathbb{E}_h[\xi_{s'}^{\text{RF}}] = |\mathcal{B}|PKr^{-\gamma}$  is the contribution at the center. Meanwhile, for the deployment in Figure 11 we have that

$$\mathbb{E}_h[\xi_{s^*}^{\text{RF}}] = \min \left( \mathbb{E}_h[\xi_{s''}^{\text{RF}}], \mathbb{E}_h[\xi_s^{\text{RF}}] \right), \quad (18)$$

where

$$\mathbb{E}_h[\xi_{s''}^{\text{RF}}] = PK \left[ x^{-\gamma} + \sum_{b=1}^{|\mathcal{B}|-1} \left[ x^2 + r^2 - 2xr \cos \left( \theta \left( b - \frac{3}{2} \right) \right) \right]^{-\frac{\gamma}{2}} \right], \quad (19)$$

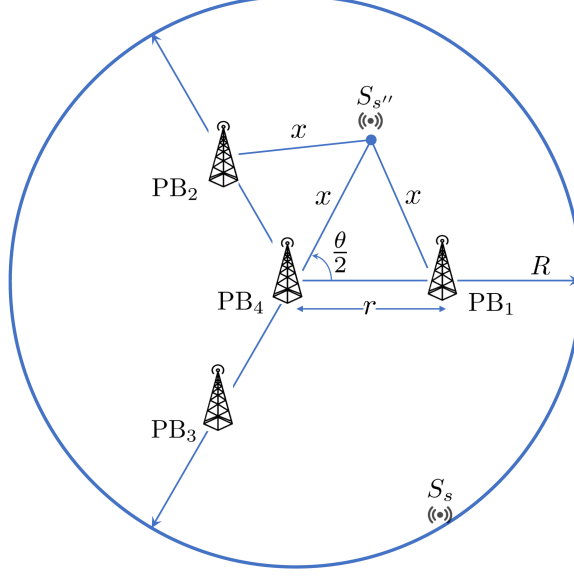


Figure 11. Example of an EC with one centered PB for  $|\mathcal{B}| = 4$  [105].

represents the contribution in a sensor equidistant to the center and two adjacent PBs at a distance  $x = r/(2 \cos \frac{\theta}{2})$  and  $\varphi = \varphi_1$ . Additionally,

$$\mathbb{E}_h[\xi_s^{\text{RF}}] = PK \left[ R^{-\gamma} + \sum_{b=1}^{|\mathcal{B}|-1} \left[ R^2 + r^2 - 2rR \cos \left( \theta \left( b - \frac{3}{2} \right) \right) \right]^{-\frac{\gamma}{2}} \right], \quad (20)$$

is the average power received at the worst sensor on the edge with  $\varphi = \varphi_1$ . Finally, the optimal positions correspond to the constellation that maximizes  $\mathbb{E}_h[\xi_s^{\text{RF}}]$  against the minimum average contribution when the network has one PB radiating from the circle center, with total power  $P_T = |\mathcal{B}|P$ , i.e.

$$r^* = \arg \max_r \left( \mathbb{E}_h[\xi_{s^*}^{\text{RF}}], |\mathcal{B}|PKR^{-\gamma} \right). \quad (21)$$

Herein,  $\mathbb{E}_h[\xi_{s^*}^{\text{RF}}]$  is defined as a parametric function using both (17) and (18), thus determined by the chosen topology. The procedure for efficiently determining  $r^*$  is detailed in the Optimal DEployment of POver BEacons (Ode-PoBes) algorithm<sup>1</sup>. Notice that  $\Delta r$  denotes the step size of the iterative search.

In general the approximation  $r \approx R \cos \frac{\theta}{2}$  holds up to  $|\mathcal{B}| = 5$  for  $\gamma = 3$ , and  $|\mathcal{B}| = 4$  for  $\gamma = 5$ , without an important degradation of the network performance, as Figure 12 depicts. As both  $|\mathcal{B}|$  and  $\gamma$  increase, the performance gap also increases, because the analytical approximation favors more the sensors in the circle's edge at the cost of degrading the contribution at the center. Moreover, the EC with one centered PB becomes better than EC without PB at the center as  $|\mathcal{B}|$  increases, having a prompt transition when  $\gamma = 5$ .

We now provide a worst-case complexity analysis for the proposed algorithm. First, for a given  $\Delta r$  the required number of iterations is  $\lfloor \frac{R}{\Delta r} \rfloor + 1$  and the maximum solution

<sup>1</sup>MatLab scripts with the implementation of Ode-PoBes algorithm are publicly available at [https://github.com/Osmel-dev/optimization\\_of\\_power\\_beacons](https://github.com/Osmel-dev/optimization_of_power_beacons)

---

**Algorithm 1** Ode-PoBes

---

```

1: Input:  $\mathcal{B}, \gamma, R, P, \Delta r$ 
2: Set  $\xi^* = |\mathcal{B}|PKR^{-\gamma}$ 
3: Set  $r^* = 0$ 
4: repeat
5:   Compute  $\mathbb{E}_h[\xi_{s^*}^{\text{RF}}]$  using both (17) and (18)
6:    $\theta^* \leftarrow \arg \max_{\theta \in \{\frac{2\pi}{|\mathcal{B}|}, \frac{2\pi}{(|\mathcal{B}|-1)}\}} (\mathbb{E}_h[\xi_{s^*}^{\text{RF}}])$ 
7:   if  $\xi^* < \max (\mathbb{E}_h[\xi_{s^*}^{\text{RF}}])$  then
8:      $\xi^* \leftarrow \max (\mathbb{E}_h[\xi_{s^*}^{\text{RF}}])$ 
9:      $r^* \leftarrow r$ 
10:  end if
11:   $r \leftarrow r + \Delta r$ 
12: until  $r \geq R$ 

```

---

error is  $\frac{\Delta r}{2}$ . Notice that the argument  $\mathbb{E}_h[\xi_s^{\text{RF}}]$  determines the computational cost of (17), and (11) proportionally scales up with  $|\mathcal{B}|$ . Similarly, each argument in (18) has a cost proportional to  $|\mathcal{B}|$ . Then, the most costly step in Ode-PoBes, step 5, requires  $\mathcal{O}(|\mathcal{B}|)$  operations, which in turn constitutes the computational cost of each iteration of the Ode-PoBes algorithm.

### 3.3.2 Interior Point Method approach (IPM)

Interior-point methods provide a framework for solving optimization problems as a sequence of equality constrained problems. The term *interior* means that the algorithm attempts starting at a feasible point and then move along the central path composed by strictly feasible points [108]. To compute the search step, IPM solves a system of gradient-based equations which demands that differentiable objective and constraints functions [109]. However, since (9a) is non-convex and highly non-linear we resort to the generalized mean approximation as an estimate of the min function [110]:

$$\min_s \mathbb{E}_h[\xi_s^{\text{RF}}] \approx \left( \frac{1}{|\mathcal{S}|} \sum_{s=1}^{|\mathcal{S}|} \xi_s^k \right)^{\frac{1}{k}}, \quad (22)$$

where  $\xi_s = \mathbb{E}_h[\xi_s^{\text{RF}}]$  is the average incident RF power at the  $s^{\text{th}}$  sensor. The approximation improves when  $k \rightarrow -\infty$  but at expense of increasing the computational cost. As alternatives, gradient-based learning algorithms utilize the softmax,  $\min_s \mathbb{E}_h[\xi_s^{\text{RF}}] \approx \frac{\sum_{s=1}^{|\mathcal{S}|} \xi_s e^{k\xi_s}}{\sum_{s=1}^{|\mathcal{S}|} e^{k\xi_s}}$  [111, eq.(7)], and the quasimax,  $\min_s \mathbb{E}_h[\xi_s^{\text{RF}}] \approx \frac{1}{k} \log \left( \sum_{s=1}^{|\mathcal{S}|} e^{k\xi_s} \right)$  [111, eq.(8)], as differentiable approximations. Here  $k$  is a real constant that determines whether the approximation tends to the minimum function ( $k < 0$ ) or to the maximum one ( $k > 0$ ). All these approximations perform alike, but since the gradient of the objective must be provided to the IPM algorithm, we adopt (22) whose derivative is more tractable.

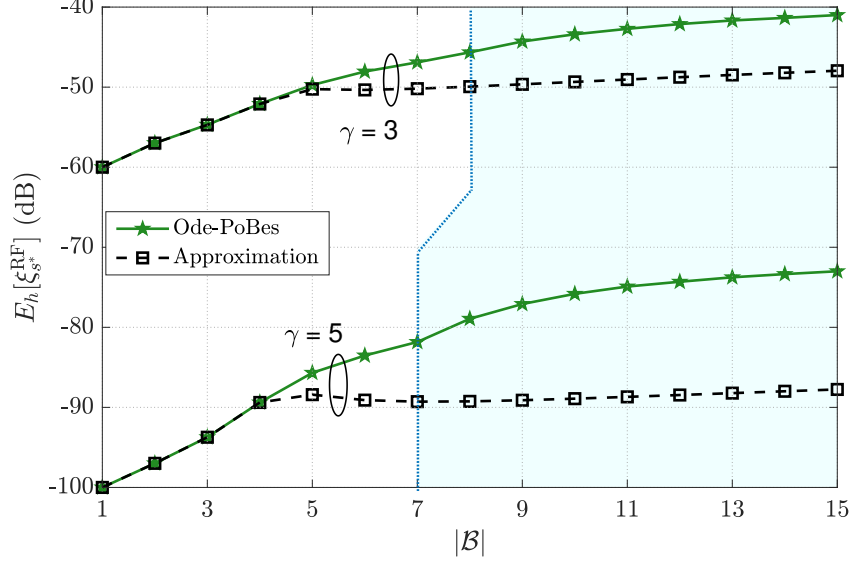


Figure 12. Performance comparison between Ode-PoBes and approximate solution vs  $|\mathcal{B}|$  for  $\gamma \in \{3, 5\}$ . The shaded region denotes the transition to the EC with one PB centered solution using Ode-PoBes solutions [105].

To turn (9b) into a set of equality constraints, we introduce a slack variable  $t_b$  such that

$$\|\mathbf{n}_b\|_2 - R + t_b = 0, \quad \forall b \in \mathcal{B}, \quad (23)$$

where  $t_b \geq 0$ ,  $\forall b \in \mathcal{B}$ . Finally, we rewrite the objective function in (9a) to include the inequality constraints of the slack variable

$$-\left(\frac{1}{|\mathcal{S}|} \sum_{s=1}^{|\mathcal{S}|} \xi_s^k\right)^{\frac{1}{k}} + \sum_{b=1}^{\mathcal{B}} \mathbb{I}[t_b] \quad (24)$$

where  $\mathbb{I}[\cdot]$  is an indicator function that takes on 0 when  $t_b \leq 0$  and  $+\infty$  otherwise, penalizing the violation of the constraint. However, this choice makes the new objective function non-differentiable due to the indicator function. Two popular differentiable approximations of the indicator function are i) the inverse barrier function,  $\mathbb{I}[t_b] \approx -\frac{1}{t_b}$  and ii) the logarithmic barrier function,  $\mathbb{I}[t_b] \approx -\mu \ln(-t_b)$ . Herein, we adopt the logarithmic barrier which is the one that comes with the IPM's implementation in the MatLab Global Optimization Toolbox. Finally, we re-cast **P2** as an equality constrained optimization problem

$$\mathbf{P2.1} : \quad \underset{\{\mathbf{n}_b\}, \{t_b\}}{\text{minimize}} \quad -\left(\frac{1}{|\mathcal{S}|} \sum_{s=1}^{|\mathcal{S}|} \xi_s^k\right)^{\frac{1}{k}} - \mu \sum_{b=1}^{|\mathcal{B}|} \ln(-t_b), \quad (25a)$$

$$\text{subject to} \quad \|\mathbf{n}_b\|_2 - R + t_b = 0, \quad \forall b \in \mathcal{B}, \quad (25b)$$

where  $\mu > 0$  must be chosen small enough to ensure accuracy of the barrier method. Next, we must solve a system of equations derived from the Karush-Kuhn-Tucker (KKT) conditions [109]

$$\nabla \mathcal{L}(\{\mathbf{n}_b\}, \{t_b\}, \boldsymbol{\lambda}) = 0, \quad \forall b \in \mathcal{B}, \quad (26)$$

$$\|\mathbf{n}_b\|^2 - R + t_b = 0, \quad \forall b \in \mathcal{B}, \quad (27)$$

where  $\mathcal{L}(\cdot)$  denotes the Lagrangian of **P2.1** given by

$$\mathcal{L}(\{\mathbf{n}_b\}, \{t_b\}, \boldsymbol{\lambda}) = -\left(\frac{1}{|\mathcal{S}|} \sum_{s=1}^{|\mathcal{S}|} \xi_s^k\right)^{\frac{1}{k}} - \mu \sum_{b=1}^{|\mathcal{B}|} \ln(-t_b) + \sum_{b=1}^{|\mathcal{B}|} \lambda_b (\|\mathbf{n}_b\|^2 - R + t_b) \quad (28)$$

and each entry of  $\boldsymbol{\lambda} = \{\lambda_b\}$  corresponds to the Lagrange multiplier associated with the  $b^{\text{th}}$  equality constraint. The partial derivatives of the Lagrangian in (26) are given by

$$\frac{\partial \mathcal{L}}{\partial \mathbf{n}_b} = \left(\frac{1}{|\mathcal{S}|} \sum_{s=1}^{|\mathcal{S}|} \xi_s^k\right)^{\frac{1-k}{k}} \frac{1}{|\mathcal{S}|} \sum_{s=1}^{|\mathcal{S}|} \xi_s^{k-1} \frac{\partial \xi_s}{\partial \mathbf{n}_b} + 2\lambda_b \mathbf{n}_b, \quad (29)$$

$$\frac{\partial \mathcal{L}}{\partial t_b} = \frac{\mu}{t_b} + \lambda_b, \quad (30)$$

where

$$\frac{\partial \xi_s}{\partial \mathbf{n}_b} = \gamma P K \|\mathbf{u}_s - \mathbf{n}_b\|_2^{-\gamma-2} (\mathbf{u}_s - \mathbf{n}_b). \quad (31)$$

Finally, IPM solves the KKT system of equations at each iteration using either Newton's method [112], or the conjugate gradient method<sup>2</sup> [113] which gives the next step towards the optimum solution. Besides, the reader must keep in mind that this method utilizes convex approximations of the objective and the constraint functions.

Figure 13 illustrates the convergence of the IPM vs  $k$  for  $|\mathcal{B}| \in \{3, 9, 15\}$  using normalized values. That is, we normalize the points of each curve with respect to  $\max_k \mathbb{E}[\xi_{s^*}^{RF}]$  for given  $\gamma$  and  $|\mathcal{B}|$ .

The reader can notice that the approximation (22) improves steadily as  $k$  decreases, except for the case  $|\mathcal{B}| = 15$  in Figure 13b that takes more effort. For the rest of the simulations we adopt  $k = -25$ , since for  $k = -30$  IPM becomes unstable for large values of the path-loss exponent, therefore compromising the reliability of the solution.

A worst-case complexity analysis for the IPM cannot be presented here. In this approach, we use the `fmincon` function of the Global Optimization Toolbox for which the worst-case complexity analysis has not been formally established. However, we do acknowledge that derivative-based methods require effort and they must deal with the existence of the derivative as the algorithm converges towards the solution. In Chapter 4 we include a time complexity plot to compare the IPM's behaviour to other methods.

### 3.3.3 Nature-inspired meta-heuristic approaches

Nature-inspired meta-heuristic approaches are stochastic gradient-based algorithms, with the capacity of dealing with non-convex, non-continuous, and non-smooth optimization problems. They find inspiration in the laws that describe our environment and distinguish from four main categories i) evolution-based, motivated by the laws of natural evolution; ii) physics-based, influenced by physical rules of natural processes; iii) swarm-based, that mimic the social behaviour of groups of animals; iv) human-based, inspired by the social behaviour of the human beings [114]. Different from gradient-based deterministic approaches such as IPMs, nature-inspired meta-heuristic algorithms provide probabilistic guarantees of finding the optimal solution, which improves as the computational time

---

<sup>2</sup>In fact, it only attempts the conjugate gradient if the Newton's method is not feasible.

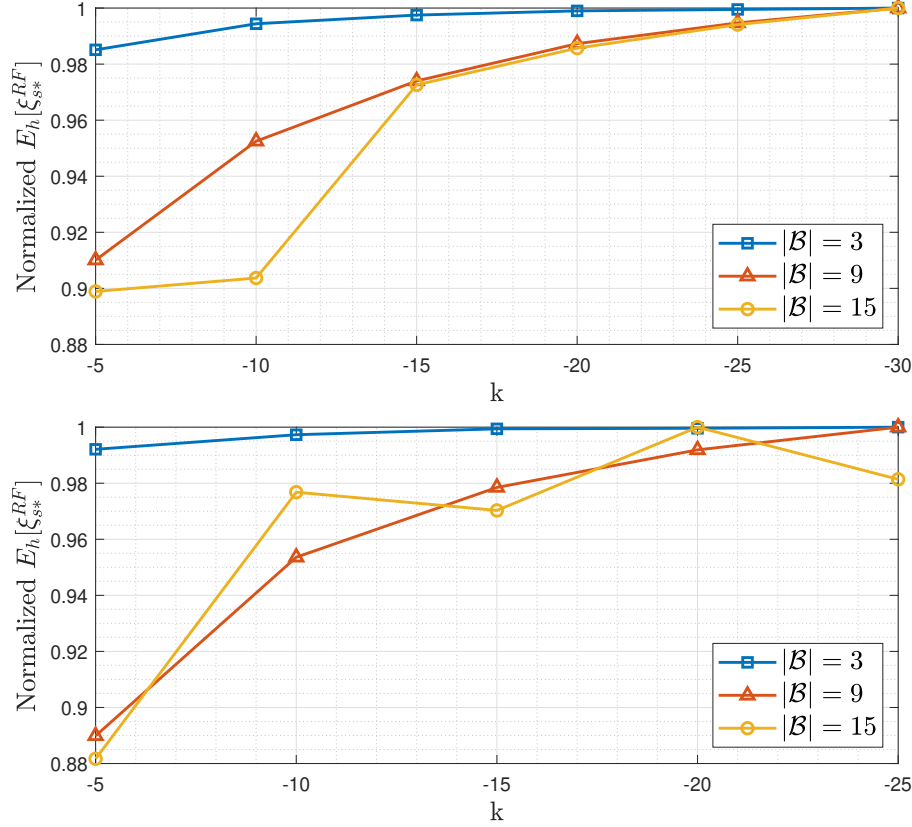


Figure 13. Normalized values of  $\mathbb{E}_h[\xi_s^{RF}]$  vs  $k$  for  $R = 100$  m and: i)  $\gamma = 3$  (top); ii)  $\gamma = 5$  (bottom).

grows larger. However, they can achieve approximate or even the optimum solution in acceptable time when tackling black box problems, extremely ill behave objective functions or large scale problems, where deterministic methods are prompt to fail (or take unreasonable time) due to combinatorial nature of these problems [115].

In particular, genetic algorithms (GAs) belong to the class of evolution-based techniques inspired by Charles Darwin's theory of natural evolution of living species [116]. Starting from an initial randomly-deployed population, GAs generate new individuals throughout selection, crossover, and mutation. At each iteration, the algorithm tests the individuals against the objective function to create the offsprings for the next population. Each individual represents a candidate solution within the solution space of the optimization problem. Some of the candidates with the highest objective function values pass directly to the next generation with the identifier of elite individuals. The individuals are also selected and combined randomly which guarantees searching the global optimum with a very low probability of getting trapped in a local optimum. The crossover fraction parameter determines the portion of the population generated either by combining or mutating the individuals in the previous generation. For instance, a crossover fraction of 0.6 means that 60% of the current population came from combining the parents in the previous generation, whereas 40 % is the result of mutation. In our particular problem, each individual contains the  $|\mathcal{B}|$  2D-coordinates corresponding to a particular solution. This approach allows us to solve **P2** directly without resorting to



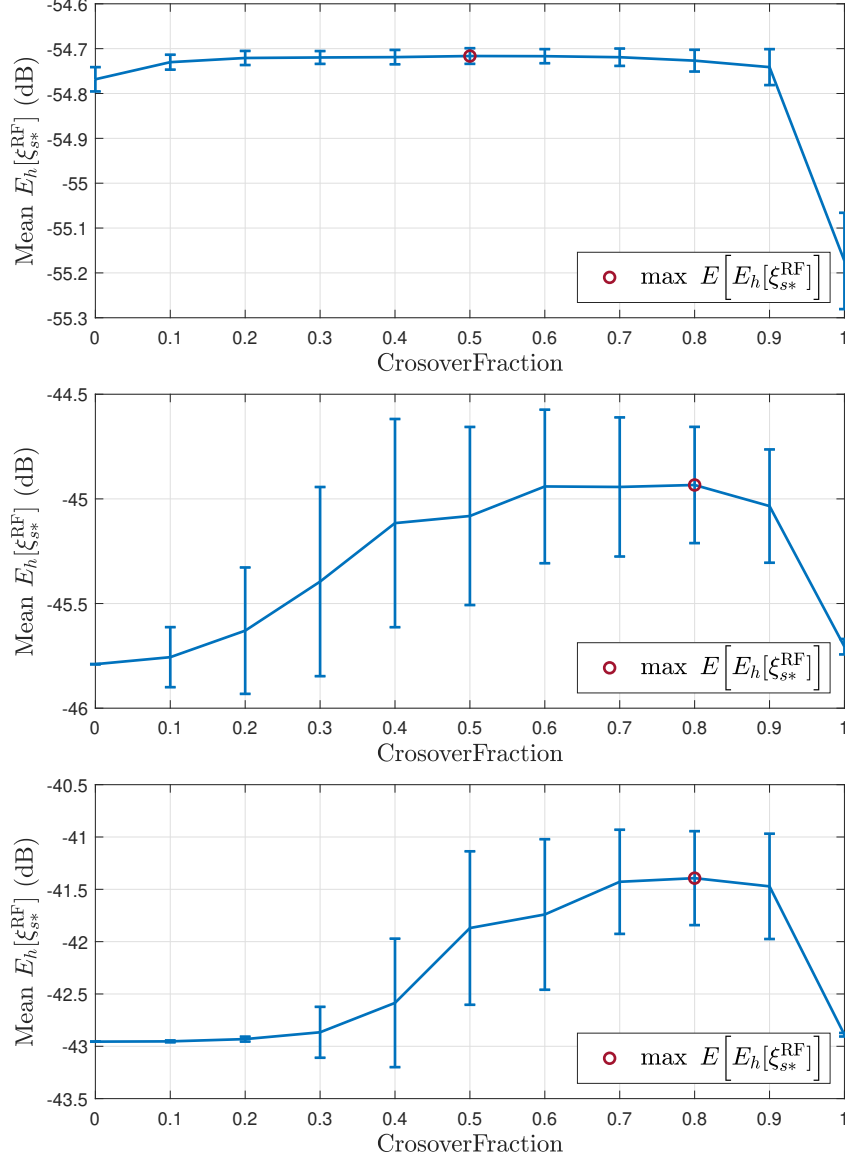


Figure 14. Mean of the objective function in **P2** using GA with a population size of 300,  $\gamma = 3$ , and for: i)  $|\mathcal{B}| = 3$  (top); ii)  $|\mathcal{B}| = 9$  (middle); and iii)  $|\mathcal{B}| = 15$  (bottom). Note that the confidence intervals ( $\pm$  the standard deviation) are also illustrated

an approximation. Figure 14 depicts the optimal objective function values versus the crossover fraction for different number of PBs.

Notice that for  $|\mathcal{B}| = 3$ , a crossover fraction of 0.5 maximizes the objective function on average, whereas for the rest of the cases the appropriate choice is 0.8. Besides, the deviation in the optimum values for a given crossover fraction becomes more relevant as  $|\mathcal{B}|$  increases. Hence, since the optimization results are quite similar for  $|\mathcal{B}| = 3$  in the selected interval, we adopt a crossover fraction of 0.8 for the rest of the simulations.

On the other hand, particle swarm optimization (PSO) is a swarm-based algorithm that mimics the behaviour of fish schooling and birds flocking [117], [118]. In PSO, a group of agent particles search for the global solution while moving in a quasi-stochastic manner inside the problem domain. For instance, consider that for the problem **P2** we

initialize the positions and velocity of a set  $\mathcal{Q}$  of agent particles. Then, at  $i^{\text{th}}$  iteration the position of the  $b^{\text{th}}$  PB at the  $q \in \mathcal{Q}$  particle is  $\{\mathbf{z}_{q,i,b} \in \mathbb{R}^{2 \times 1} | \forall b \in \mathcal{B}\}$ . Therefore, each particle's position comprises a candidate solution in **P2**. Let us define the objective function as

$$f_{\text{PSO}}(\{\mathbf{z}_{q,i,b} | \forall b \in \mathcal{B}\}) = \min_s \mathbb{E}[\xi_s^{RF}] - \epsilon \sum_{b=1}^{|\mathcal{B}|} \frac{1}{\|\mathbf{z}_{q,i,b}\|_2 - R}, \quad (32)$$

where  $\mathbb{E}[\xi_s^{RF}]$  is computed according with (8) but replacing  $\mathbf{n}_b$  for  $\mathbf{z}_{q,i,b}$ , and the second term corresponds to the approximation of the indicator function

$$\mathbb{I}(\|\mathbf{z}_{q,i,b}\|_2 - R) \approx -\frac{1}{\|\mathbf{z}_{q,i,b}\|_2 - R}, \quad \forall b \in \mathcal{B}, \quad (33)$$

whose impact on the problem solution is limited by making  $\epsilon \rightarrow 0$ . Herein, we choose this approximation since it exhibits better results compared with the logarithmic barrier function when using PSO. At the iteration  $i'$ , the particles update their position and velocity considering their initial values, local best position  $\text{pbest}(q, i')$ , and the global best position  $\text{gbest}(q)$  [118], where

$$\begin{aligned} \text{pbest}(q, i') &= \arg \min_{i=1,2,\dots,i'} f_{\text{PSO}}(\{\mathbf{z}_{q,i,b} | \forall b \in \mathcal{B}\}), \quad \forall q \in \mathcal{Q} \\ \text{gbest}(q) &= \arg \min_{\substack{i=1,2,\dots,i' \\ \forall q \in \mathcal{Q}}} f_{\text{PSO}}(\{\mathbf{z}_{q,i,b} | \forall b \in \mathcal{B}\}), \end{aligned}$$

to find the best of all local solutions until the objective no longer improves. In this case, we keep the default parameter values of the algorithm since the optimization results don't change significantly as we tune them.

Despite the advantages, a rigorous mathematical analysis for metaheuristic algorithms remains as an open problem and due to its stochastic nature, the complexity may vary even for the same problem [119], [120]. Moreover, in the majority of nature-inspired metaheuristic algorithms, the complexity doesn't necessarily scale with the size of the optimization problem. Hence, the analysis of convergence and efficiency becomes challenging. For these reasons, in Chapter 4 we present a time-convergence analysis concerning the number of PBs in the network, which gives us an idea of how each algorithm scales with the size of the problem.

### 3.4 Algorithm for optimal deployment and practical considerations

Once **P2** is solved, one needs to minimize the number of deployed PBs that satisfies the energy outage probability requirement in (7b). Algorithm 2 shows the iterative procedure for finding the minimum  $|\mathcal{B}|$ . At each iteration, **P2** is solved until the energy outage condition is guaranteed. Remember that the distribution of  $\xi_s^{\text{RF}}$  obeys (6). In the next chapter, we present optimal deployment results under different network conditions.

In practice, the performance of the algorithm for finding the PBs' positions depends on how well the path loss model fits the actual conditions. For instance, recent measurement campaigns in wireless sensor networks corroborate the dependence of the path loss exponent on the environment's characteristics [121]. Hence, different sub-regions of the

---

**Algorithm 2** Computation of the minimum  $|\mathcal{B}|$ 


---

```

1: Input:  $\gamma, R, P_T, \Delta r, \xi_0, \zeta$ 
2: Set  $|\mathcal{B}| = 1$ 
3: while  $\mathbb{P}[\xi_s^{\text{RF}} \leq \xi_0] > \zeta$  do
4:    $|\mathcal{B}| \leftarrow |\mathcal{B}| + 1$ 
5:    $P \leftarrow \frac{P_T}{|\mathcal{B}|}$ 
6:   Solve P2
7: end while

```

---

network might require different path loss models. Moreover, the inherent properties of IoT networks (e.g. small antenna heights, low transmission power, and stationary nodes) limit the applicability of traditional propagation models [122]. Similarly, the proposed algorithm framework guarantees meeting the energy outage requirement provided the channel fading distribution is accurately known beforehand.

Therefore, opportunistically selecting appropriate channel models, at both large (path-loss) and small scale (fading distribution), is essential. Machine learning methods are potential candidates for such a task, that must also provide confidence when a large set of measurements is available [123]. The risk of channel modeling/prediction errors must be taken into account in the optimization framework as well. Finally, we can utilize the solutions from Ode-PoBes as a good initial guess for any of the metaheuristic algorithms before treated, which can improve the performance of the final deployment.

## 4 NUMERICAL RESULTS

In this chapter, we present optimal PBs deployments that satisfy a certain energy outage constraint under different channel state conditions. Moreover, we compare the proposed methods for optimizing the PBs' positions in terms of minimum average incident RF power as well as the required computational time. Finally, we provide insights on the maximum coverage area that can be served by a certain number of PBs and the impact of having multiple antennas at the PBs. By default, we use the simulation parameters listed in Table 4.

### 4.1 On the optimal PBs' positions

Figure 15 shows the optimal PBs' positions after solving **P2** for different number of PBs using IPM; while the heat map represents the average power levels along the circular area.

The reader can notice that the optimal PBs' positions form concentric circumferences with more rings as the number of PB increases. This supports our intuition when using the EC strategies in Ode-PoBes algorithm. Besides, the average power distribution gets more homogeneous as more PBs are deployed, which means that the dimensions of the regions with very weak incident power decrease. Moreover, observe from Figure 16 that the average incident power at the worst sensor  $\mathbb{E}[\xi_{s^*}^{RF}]$  improves when  $|\mathcal{B}|$  increases according to the optimization methods proposed in Chapter 3. Here, as a benchmark, we also present the case of a centered PB radiating with total power  $P_T$ , which is equivalent to place all  $|\mathcal{B}|$  PBs at the center, each transmitting with power  $\frac{P_T}{|\mathcal{B}|}$ .

For  $|\mathcal{B}| \geq 3$  all optimization methods outperform the benchmark centered PB, while the performance gap increases as we optimally distribute more PBs. The special case  $|\mathcal{B}| = 2$  is equivalent to place a single PB at the circle center, with twice the transmit power as evidenced by the optimization output of all the methods. In particular, Ode-PoBes and IPM stand out over the others in terms of convergence stability towards the final solution. Notice that for  $\gamma = 5$  the curve bends at  $|\mathcal{B}| = 7$ , which means that all methods agree with the transition to the EC with one PB centered deployment. Herein, we limit the optimization to 15 PBs due to the poor convergence of GAs compared with

Table 4. Default simulation parameters.

Parameter	Value
$R$	100 m
$P_T$	10 W
$\xi_0$	-22 dBm
$K$	1
$ \mathcal{S} $	1000 sensors
$\gamma$	3
$\kappa$	3
$\epsilon$	0.2
$k$	-25

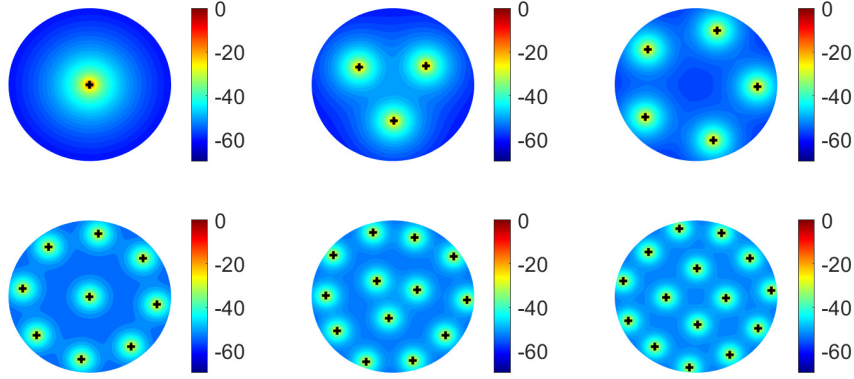


Figure 15. Heat map of the available average power in the circle area for  $|\mathcal{B}| \in \{1, 3, 5, 9, 13, 15\}$  and  $P_T = 1$ . The black crosses represent the optimal PBs' positions.

the IPM approach when the number of PBs increases above 15. In this case, the classical GAs approach doesn't converge steadily towards the desired solution as the complexity of the problem increases. In contrast, PSO offers a more stable outcome compared with IPM as a reference.

With Ode-PoBes, we obtain topologies that follow the general trend of the ones with the IPM but with less computational cost. In fact, as Ode-PoBes searches for the optimum positioning, it doesn't require the computation of partial derivative or solving large systems of linear equations. Figure 17 depicts the normalized average convergence time for all methods with respect to the time required for Ode-PoBes. Notice that the Ode-PoBes algorithm is superior by four order of magnitude since it reduces the dimension of the optimization variable. For instance, assume that  $|\mathcal{B}| = 15$ . Then, while GAs/PSO deals with individuals/particles of size  $15 \times 2$ , and IPM must find 15 2D coordinates plus 15 slack variables and 15 Lagrange multipliers, Ode-PoBes just solves the optimum pair of scalars  $(r^*, \theta^*)$ . However, this fact impacts less the nature-inspired meta-heuristic algorithms, showing the gain of the stochastic gradient optimization over the IPM. Indeed, the stochastic gradient method updates all optimization variables by estimating the gradient over a randomly selected subset of individuals/particles at each iteration. However, the average time gap decreases as  $|\mathcal{B}|$  increases, i.e. as the number of possible constellations increases. Finally, for  $|\mathcal{B}| \geq 7$  the nature-inspired algorithms approaches exhibit a close performance.

## 4.2 On the optimal solutions of P1

Let us consider a wireless charging service scenario where each PB takes the power from an external wired source for charging the IoT sensors. In order to obtain profits, the service provider chooses to distribute a fixed power budget of  $P_T = 10$  W among the individual PBs according to (7c). Figure 18 depicts the energy outage probability vs  $|\mathcal{B}|$ , when solving the problem **P2** with IPM and Ode-PoBes algorithms. Hereinafter, IPM will be our benchmark strategy provided its accuracy over GA and PSO. The monotonic decrease of the energy outage probability for both approaches proves the effectiveness of the distributed PBs approach when improving the network reliability.

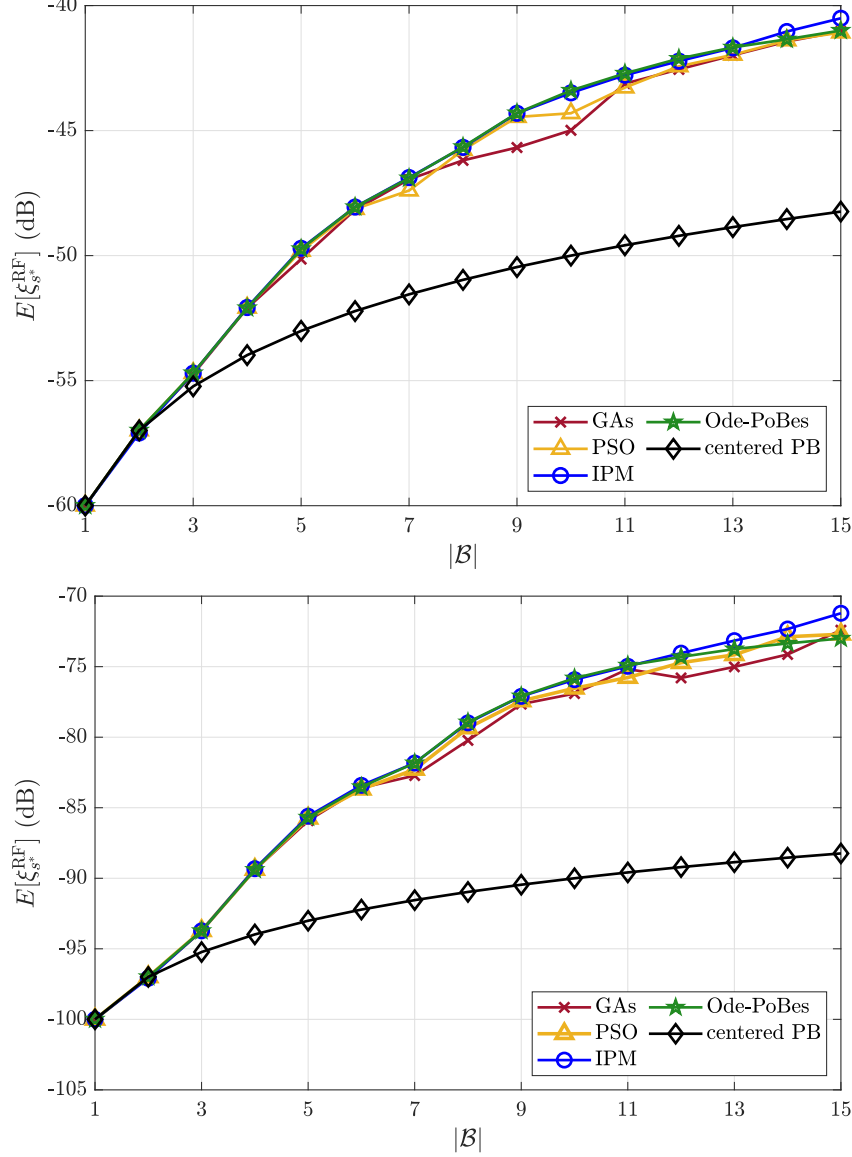


Figure 16. Available average power at the worst position for optimal PB placement,  $P = 1$ , and:  $\gamma = 3$  (top),  $\gamma = 5$  (bottom) [105].

For this setup, we also present the solutions of **P1** in Figure 19 as a function of  $\zeta$  and  $R$ . Figure 19 (left) depicts a stable increment in the number of PBs needed to meet the target QoS constraint as the network gets larger; whereas Figure 19 (right) shows that tight QoS agreements demand the deployment of more PBs. In general, the fluctuations in the number of PBs indicate that the distance-dependent loss has a dominant impact on the optimal solutions of **P1**. Notice that Ode-PoBes outperforms IPM's solutions when serving larger areas with tight probabilistic energy outage requirements. For instance, Ode-PoBes finds an optimal deployment with 4 PBs less than IPM when  $R = 100$  m.

The difference between Ode-PoBes and IPM with respect to the required PBs is a consequence of the numerical approximations that affect the symmetry of the final solution. In fact, IPM solves  $|\mathcal{B}|$  individual positions within the space of possible constellations, which doesn't guarantee symmetric layers with respect to the origin.

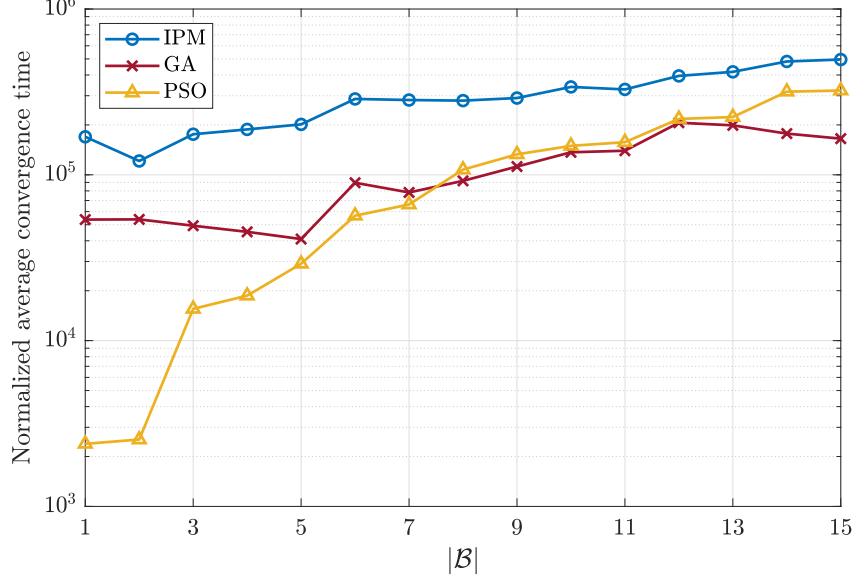


Figure 17. Normalized average convergence time vs  $|\mathcal{B}|$  [105].

Meanwhile, Ode-PoBes finds  $(r^*, \theta^*)$  that maximizes the  $\mathbb{E}[\xi_{s^*}^{\text{RF}}]$  using EC symmetric constellations. Based of these observations, we conclude that the symmetry of the deployments determines, over the number of PBs, the ultimate performance of the worst-positioned IoT sensor.

### 4.3 On the maximum coverage area

Now, consider the same scenario as in the previous section but let us focus on the maximum coverage area with respect to  $\mathbb{E}[\xi_{s^*}^{\text{RF}}]$  using the minimum average incident RF power obtained with Ode-PoBes. As illustrated in Fig. 20, a the distributed deployment allows serving larger areas than the centered PB approach, and the performance gap increases with the number of PBs and the path-loss exponent. Notice that bringing the PBs closer to the worst-positioned sensors impacts stronger on the average incident RF power than increasing the power in a centered PB. In fact,  $\xi_s^{\text{RF}}$  is a linear function of the transmit power  $P$ , but depends exponentially on the distance  $d_{s,b}$ . Besides, as the sensitivity  $\xi_0$  of the harvesting circuitry increases, not just the coverage area but the gap among different PBs' topologies diminish. That is, as we distribute the power budget among an increasing number of PBs, the received power at reference distance of 1 m decreases by a factor of  $|\mathcal{B}|$  with respect to the centered PB approach, and thus the incident power at the worst position. An interesting result is that our proposal allows extending the coverage area without increasing the level of RF-EMF in the proximity of the PBs. For the sake of clarity, we have highlighted some points ( $|\mathcal{B}| \in \{3, 7, 10\}$ ) in Figure 20 (top), so that the readers can check the correspondence with the results in Figure 20 (bottom), both when  $\xi_0 = -22$  dBm.

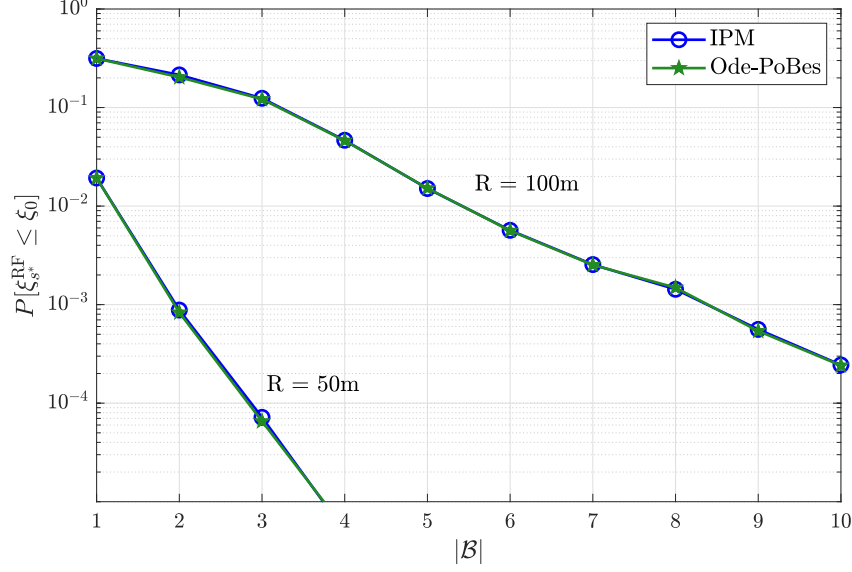


Figure 18. Energy outage probability vs  $|\mathcal{B}|$ , for  $R \in \{50, 100\}$  m [105].

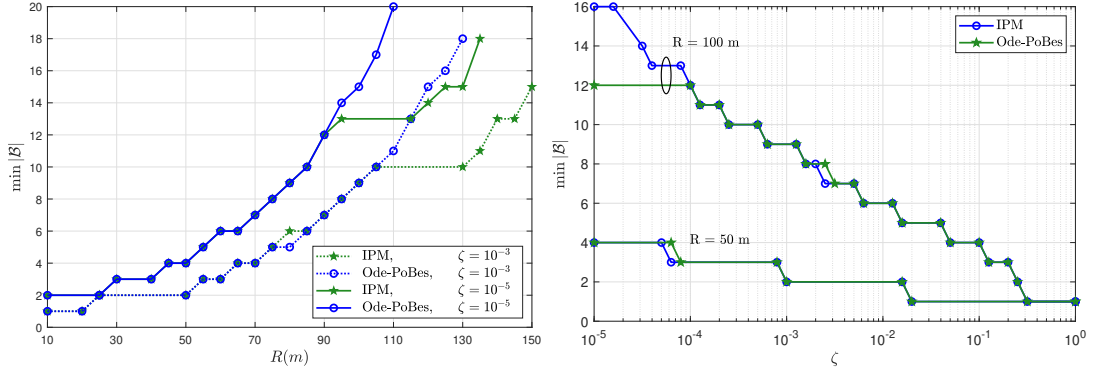


Figure 19. Solutions of **P1** using Ode-PoBes and IPM [105]: i)  $\min |\mathcal{B}|$  vs  $R$  for  $\zeta \in \{10^{-3}, 10^{-5}\}$  (left); ii)  $\min |\mathcal{B}|$  network reliability  $\zeta$  for  $R \in \{50, 100\}$  m (right).

#### 4.4 On CSI-free multi-antenna WET

The authors in [57] analyzed the performance of multiple-antenna strategies for powering a massive number of EH devices using

- i) one antenna (OA), in which the PB transmits with full power using a single antenna out of the whole array to charge the sensors. If the CSI is available, the PB uses the antenna that maximizes the EH;
- ii) all antennas at once (AA), in which the PB transmits with all antennas simultaneously. If the CSI is available, the optimal strategy is to perform energy beamforming, otherwise the PB splits equally the power among the antennas;
- iii) switching antennas (SA) schemes, in which the PB transmits with full power by one antenna at the time, in a way that the whole array is utilized within a channel coherence block;



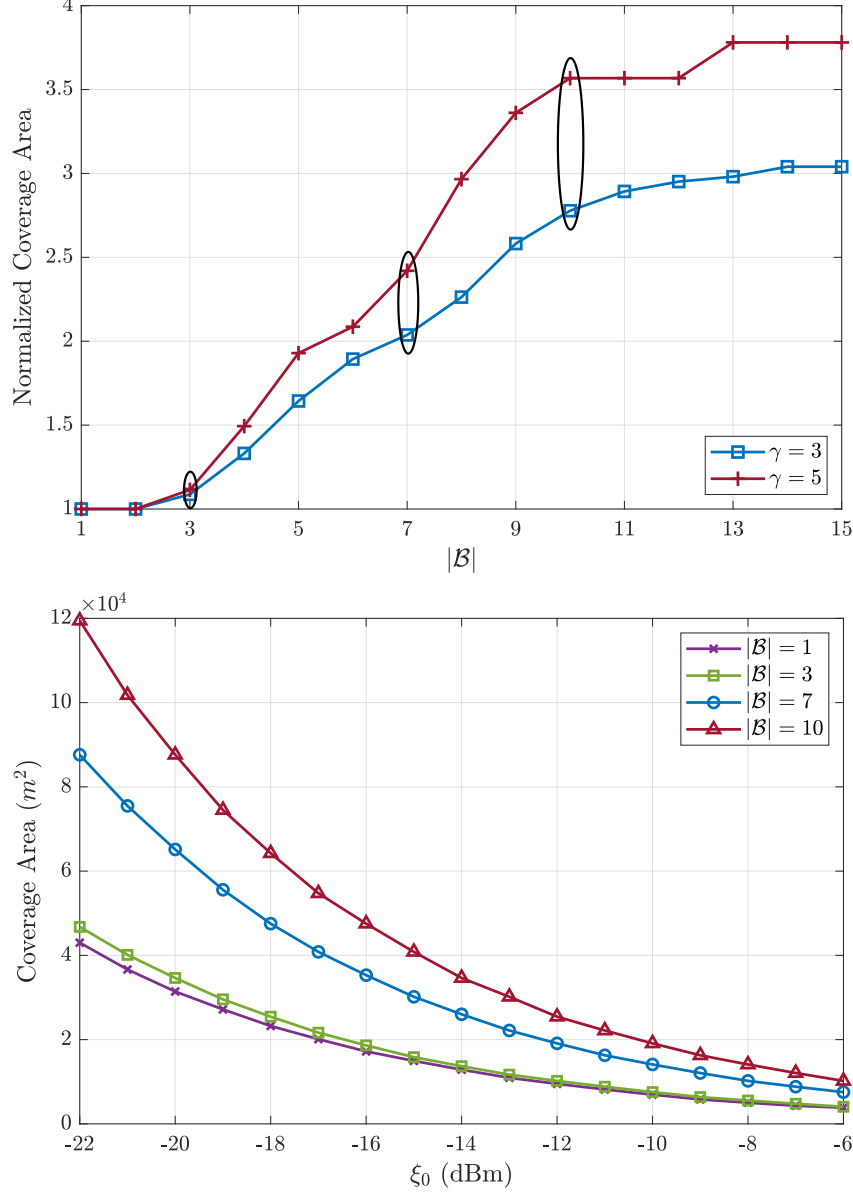


Figure 20. Maximum coverage area results [105]: i) Normalized to the maximum coverage area with a centered PB vs  $|\mathcal{B}|$  for  $\gamma \in \{3, 5\}$  (top); ii) Coverage area vs  $\xi_0$  for  $|\mathcal{B}| \in \{1, 3, 7, 10\}$  (bottom).

Herein, we only focus on the CSI-free SA scheme given that OA can be seen as an special case when only a single antenna is used. On the other hand, the performance claimed for the CSI-free AA in [57] is valid only for equal mean phases along the transmit antennas, which is difficult to hold in practice. Besides, SA preserves the harvested energy as in the case of single-antenna PBs (although boosting the energy diversity), while the variance is a function of the spatial correlation among the antennas.

For this setup, let us consider that each PB is equipped with  $A$  antennas. The use of SA scheme, as Figure 21 depicts, improves the system performance in terms of reducing the outage probability at the worst sensor as the number of antennas increases. As an example, we constraint the system to  $\zeta = 10^{-4}$ , and it can be observed that the

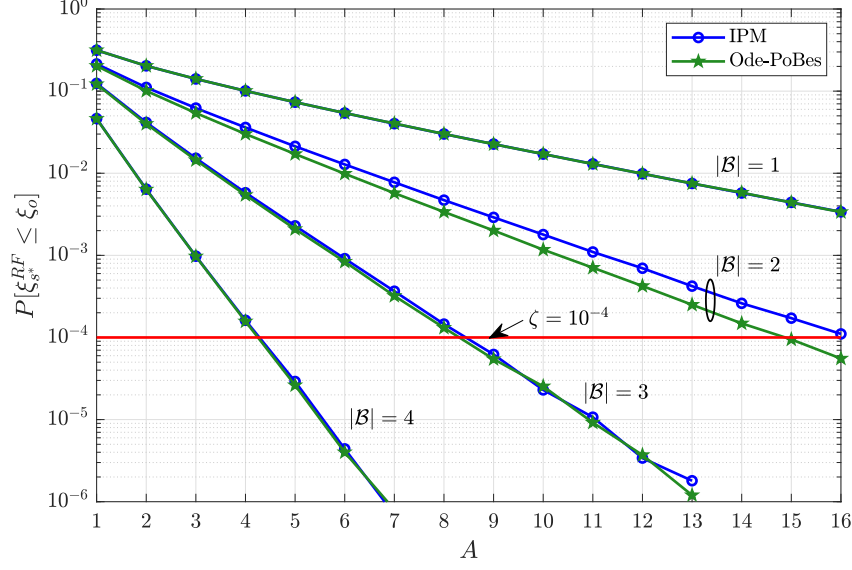


Figure 21. Energy outage probability versus number of antennas, for  $|\mathcal{B}| \in \{1, 2, 3, 4\}$  [105].

number of PBs have a greater impact on the system performance than the number of antennas. In fact, the outage probability does not improve significantly as the number of antennas increases when  $|\mathcal{B}| = 1$ , but once more PBs are distributed in the network, the performance impact of the number of antennas grows significantly. The reader can observe that doubling the number of antennas per PB can be roughly equivalent to keep the same number of antennas per-PB but deploying an additional PB.

## 5 CONCLUSIONS

In this thesis, we reviewed the most common WET-enabled networks models, and some of the techniques that may realize WET as an efficient technology for wirelessly powering the coming green IoT networks. Besides, we discussed the role of EH from ambient sources to sustain sensors' networks. Moreover, we studied the optimal deployment of PBs to meet a probabilistic energy outage constraint when powering massive IoT network. We considered scenarios where PBs couldn't afford CSI acquisition and the sensors' positions were unknown. We provided analytical insights on the optimal PBs' positions by placing them equally-far-from-center; and further, we proposed a linear-time algorithm for solving this problem. For comparison, we used an interior-point method based on the logarithmic barrier function and nature-inspired meta-heuristic algorithms to compute the optimal PBs's positions. In the former approach we took advantage of the generalized mean as a differentiable approximation of objective function, whereas for the others, we solved the optimization problem directly. Finally, we discussed the practicalities for implementing the proposed algorithm in different scenarios.

Numerical experiments demonstrated that our algorithm converges faster than the benchmark methods, and meets the energy outage requirement with a smaller number of PBs to be deployed. We also showed that optimally distributed PBs can serve wider areas than the naive centered PB approach using the same total transmit power. Besides, we demonstrated that the optimal PB deployment depends mostly on the distance-dependent loss, and more PBs are required as the radius of the area or the energy outage requirements increase. The comparison among the optimization methods showed the strong impact of the deployment symmetry on the average incident power at the worst-positioned sensor. At the end, we presented results using multi-antenna PBs that exploit a CSI-free WET scheme. We found that although an increasing number of antennas per PB reduces the probability of energy outage, the number of deployed PBs impacts stronger the system performance. For instance, considering the same total power, the performance obtained when doubling the number of antennas at the PBs can be alternatively attained by properly deploying an additional PB which reduces the hardware complexity. Our results provide valuable insights for designing practical WET setups by answering how many PBs are needed, and their corresponding locations, for powering certain area with a certain average RF power availability or energy outage QoS constraints.

## 6 REFERENCES

- [1] Mahmood N.H., Böcker S., Munari A., Clazzer F., Moerman I., Mikhaylov K., Lopez O., Park O.S., Mercier E., Bartz H., Jäntti R., Pragada R., Ma Y., Annanperä E., Wietfeld C., Andraud M., Liva G., Chen Y., Garro E., Burkhardt F., Alves H., Liu C.F., Sadi Y., Dore J.B., Kim E., Shin J., Park G.Y., Kim S.K., Yoon C., Anwar K. & Seppänen P. (2020), White paper on critical and massive machine type communication towards 6G.
- [2] Mahapatra R., Nijssure Y., Kaddoum G., Ul Hassan N. & Yuen C. (2016) Energy efficiency tradeoff mechanism towards wireless green communication: A survey. *IEEE Communications Surveys Tutorials* 18, pp. 686–705.
- [3] López O.L.A., Alves H., Souza R.D., Montejo-Sanchez S., Fernandez E.M.G. & Latva-aho M. (2021) Massive wireless energy transfer: Enabling sustainable IoT towards 6G era. *IEEE Internet of Things Journal* , pp. 1–1.
- [4] Zigbee. URL: <https://zigbeealliance.org/solution/zigbee/>.
- [5] Bluetooth Radio Versions. URL: <https://www.bluetooth.com/learn-about-bluetooth/radio-versions/>.
- [6] Shelby Z. & Bormann C. (2011) 6LoWPAN: The wireless embedded Internet, vol. 43. John Wiley & Sons.
- [7] Kwak K.S., Ullah S. & Ullah N. (2010) An overview of IEEE 802.15.6 standard. In: 3rd International Symposium on Applied Sciences in Biomedical and Communication Technologies (ISABEL 2010), IEEE, pp. 1–6.
- [8] Banks A., Briggs E., Borgendale K. & Gupta R.G. (2019), MQTT Version 5.0. URL: <https://docs.oasis-open.org/mqtt/mqtt/v5.0/os/mqtt-v5.0-os.html>.
- [9] Cetinkaya O., Balsamo D. & Merrett G.V. (2020) Internet of MIMO Things: UAV-assisted wireless-powered networks for future smart cities. *IEEE Internet of Things Magazine* 3, pp. 8–13.
- [10] Carrano R.C., Passos D., Magalhaes L.C.S. & Albuquerque C.V.N. (2014) Survey and taxonomy of duty cycling mechanisms in wireless sensor networks. *IEEE Communications Surveys Tutorials* 16, pp. 181–194.
- [11] Moody J., Bassirian P., Roy A., Liu N., Barker N.S., Calhoun B.H. & Bowers S.M. (2019) Interference robust detector-first near-zero power wake-up receiver. *IEEE Journal of Solid-State Circuits* 54, pp. 2149–2162.
- [12] López O.L.A., Mahmood N.H., Alves H., Lima C.M. & Latva-aho M. (2020) Ultra-low latency, low energy, and massiveness in the 6G era via efficient CSIT-limited scheme. *IEEE Communications Magazine* 58, pp. 56–61.
- [13] Rault T., Bouabdallah A. & Challal Y. (2014) Energy efficiency in wireless sensor networks: A top-down survey. *Computer Networks* 67, pp. 104–122.

- [14] Phan K., Le L., Vorobyov S. & Le-Ngoc T. (2009) Power allocation and admission control in multiuser relay networks via convex programming: centralized and distributed schemes. *EURASIP Journal on Wireless Communications and Networking* 2009, pp. 1–12.
- [15] Jiang D., Li W. & Lv H. (2017) An energy-efficient cooperative multicast routing in multi-hop wireless networks for smart medical applications. *Neurocomputing* 220, pp. 160–169.
- [16] Das S.K. & Tripathi S. (2018) Intelligent energy-aware efficient routing for MANET. *Wireless Networks* 24, pp. 1139–1159.
- [17] Jesus P., Baquero C. & Almeida P.S. (2015) A survey of distributed data aggregation algorithms. *IEEE Communications Surveys Tutorials* 17, pp. 381–404.
- [18] Pushpalatha S. & Shivaprakasha K. (2020) Energy-efficient communication using data aggregation and data compression techniques in wireless sensor networks: A survey. In: *Advances in Communication, Signal Processing, VLSI, and Embedded Systems*, Springer, pp. 161–179.
- [19] Soua R. & Minet P. (2011) A survey on energy efficient techniques in wireless sensor networks. In: *4th Joint IFIP Wireless and Mobile Networking Conference (WMNC)*, pp. 1–9.
- [20] Al-Hawri E., Correia N. & Barradas A. (2019) Design of network coding based reliable sensor networks. *Ad Hoc Networks* 91, p. 101870.
- [21] Luo P., Peng D., Wang Y. & Zheng X. (2018) Review of solar energy harvesting for IoT applications. In: *IEEE Asia Pacific Conference on Circuits and Systems (APCCAS)*, pp. 512–515.
- [22] Champier D. (2017) Thermoelectric generators: A review of applications. *Energy Conversion and Management* 140, pp. 167–181.
- [23] Piggot A.J. (2020), System and method for wireless power transfer using thermoelectric generators. US Patent App. 16/705,985.
- [24] Hou L., Tan S., Zhang Z. & Bergmann N.W. (2018) Thermal energy harvesting WSNs node for temperature monitoring in IIoT. *IEEE Access* 6, pp. 35243–35249.
- [25] Adu-Manu K.S., Adam N., Tapparello C., Ayatollahi H. & Heinzelman W. (2018) Energy-harvesting wireless sensor networks (EH-WSNs): A review. *ACM Transactions on Sensor Networks (TOSN)* 14. URL: <https://doi.org/10.1145/3183338>.
- [26] Sekander S., Tabassum H. & Hossain E. (2020) Statistical performance modeling of solar and wind-powered UAV communications. *IEEE Transactions on Mobile Computing* , pp. 1–1.
- [27] Fahmy H.M.A. (2020) *Energy Harvesting in WSNs*, Springer International Publishing, Cham. pp. 41–99. URL: [https://doi.org/10.1007/978-3-030-29700-8\\_2](https://doi.org/10.1007/978-3-030-29700-8_2).

- [28] Hu J., Yang K., Wen G. & Hanzo L. (2018) Integrated data and energy communication network: A comprehensive survey. *IEEE Communications Surveys and Tutorials* 20, pp. 3169–3219.
- [29] Piñuela M., Mitcheson P.D. & Lucyszyn S. (2013) Ambient RF energy harvesting in urban and semi-urban environments. *IEEE Transactions on Microwave Theory and Techniques* 61, pp. 2715–2726.
- [30] Kim S., Vyas R., Bito J., Niotaki K., Collado A., Georgiadis A. & Tentzeris M.M. (2014) Ambient RF energy harvesting technologies for self-sustainable standalone wireless sensor platforms. *Proceedings of the IEEE* 102, pp. 1649–1666.
- [31] Kwan J.C. & Fapojuwo A.O. (2016) Measurement and analysis of available ambient radio frequency energy for wireless energy harvesting. In: *IEEE 84th Vehicular Technology Conference (VTC-Fall)*, pp. 1–6.
- [32] Saab S., Kouzayha N., Eid A., Benbuk A.A., Costantine J. & Dawy Z. (2020) Recycling ambient Wi-Fi signals for low energy wake-up of wireless sensors. *IEEE Sensors Letters* 4, pp. 1–4.
- [33] Vu H.S., Nguyen N., Ha-Van N., Seo C. & Thuy Le M. (2020) Multiband ambient RF energy harvesting for autonomous IoT devices. *IEEE Microwave and Wireless Components Letters* 30, pp. 1189–1192.
- [34] Mishu M.K., Rokonuzzaman M., Pasupuleti J., Shakeri M., Rahman K.S., Hamid F.A., Tiong S.K. & Amin N. (2020) Prospective efficient ambient energy harvesting sources for IoT-equipped sensor applications. *Electronics* 9, p. 1345.
- [35] Amer A.A.G., Sapuan S.Z., Nasimuddin N., Alphones A. & Zinal N.B. (2020) A comprehensive review of metasurface structures suitable for RF energy harvesting. *IEEE Access* 8, pp. 76433–76452.
- [36] Osorio de la Rosa E., Vázquez Castillo J., Carmona Campos M., Barbosa Pool G.R., Becerra Nuñez G., Castillo Atoche A. & Ortegón Aguilar J. (2019) Plant microbial fuel cells-based energy harvester system for self-powered IoT applications. *Sensors* 19, p. 1378.
- [37] Weddell A.S., Magno M., Merrett G.V., Brunelli D., Al-Hashimi B.M. & Benini L. (2013) A survey of multi-source energy harvesting systems. In: *2013 Design, Automation Test in Europe Conference Exhibition (DATE)*, pp. 905–908.
- [38] Zeng Y., Clerckx B. & Zhang R. (2017) Communications and signals design for wireless power transmission. *IEEE Transactions on Communications* 65, pp. 2264–2290.
- [39] Chen Y. & Chiu C. (2017) Maximum achievable power conversion efficiency obtained through an optimized rectenna structure for RF energy harvesting. *IEEE Transactions on Antennas and Propagation* 65, pp. 2305–2317.

- [40] Song C., Huang Y., Carter P., Zhou J., Joseph S.D. & Li G. (2018) Novel compact and broadband frequency-selectable rectennas for a wide input-power and load impedance range. *IEEE Transactions on Antennas and Propagation* 66, pp. 3306–3316.
- [41] Cansiz M., Altinel D. & Kurt G.K. (2019) Efficiency in RF energy harvesting systems: A comprehensive review. *Energy* 174, pp. 292–309.
- [42] Lin W. & Ziolkowski R.W. (2020) A circularly polarized wireless power transfer system for Internet-of-Things applications. In: 4th Australian Microwave Symposium (AMS), pp. 1–2.
- [43] Boaventura A., Collado A., Carvalho N.B. & Georgiadis A. (2013) Optimum behavior: Wireless power transmission system design through behavioral models and efficient synthesis techniques. *IEEE Microwave Magazine* 14, pp. 26–35.
- [44] Clerckx B., Zhang R., Schober R., Ng D.W.K., Kim D.I. & Poor H.V. (2019) Fundamentals of wireless information and power transfer: From RF energy harvester models to signal and system designs. *IEEE Journal on Selected Areas in Communications* 37, pp. 4–33.
- [45] Wu Q., Zhang G., Ng D.W.K., Chen W. & Schober R. (2019) Generalized wireless-powered communications: When to activate wireless power transfer? *IEEE Transactions on Vehicular Technology* 68, pp. 8243–8248.
- [46] Krikidis I. (2019) Average age of information in wireless powered sensor networks. *IEEE Wireless Communications Letters* 8, pp. 628–631.
- [47] Zheng Y., Bi S., Zhang Y.J., Quan Z. & Wang H. (2020) Intelligent reflecting surface enhanced user cooperation in wireless powered communication networks. *IEEE Wireless Communications Letters* 9, pp. 901–905.
- [48] Azarhava H. & Musevi Niya J. (2020) Energy efficient resource allocation in wireless energy harvesting sensor networks. *IEEE Wireless Communications Letters* 9, pp. 1000–1003.
- [49] Lu P., Song C. & Huang K.M. (2020) A compact rectenna design with wide input power range for wireless power transfer. *IEEE Transactions on Power Electronics* 35, pp. 6705–6710.
- [50] Lin W., Ziolkowski R.W. & Huang J. (2019) Electrically small, low-profile, highly efficient, huygens dipole rectennas for wirelessly powering Internet-of-Things devices. *IEEE Transactions on Antennas and Propagation* 67, pp. 3670–3679.
- [51] Lin W. & Ziolkowski R.W. (2020) Electrically small huygens CP rectenna with a driven loop element maximizes its wireless power transfer efficiency. *IEEE Transactions on Antennas and Propagation* 68, pp. 540–545.
- [52] Alja'afreh S.S., Song C., Huang Y., Xing L. & Xu Q. (2020) A dual-port, dual-polarized and wideband slot rectenna for ambient RF energy harvesting. In: 14th European Conference on Antennas and Propagation (EuCAP), pp. 1–5.

- [53] Reed R., Pour F.L. & Ha D.S. (2020) An efficient 2.4 GHz differential rectenna for radio frequency energy harvesting. In: IEEE 63rd International Midwest Symposium on Circuits and Systems (MWSCAS), pp. 208–212.
- [54] Zhao J., Subramanyam G. & Yue H. (2020) A dual-band rectifying antenna design for RF energy harvesting. In: IEEE 63rd International Midwest Symposium on Circuits and Systems (MWSCAS), pp. 415–418.
- [55] Boshkovska E., Ng D.W.K., Zlatanov N. & Schober R. (2015) Practical non-linear energy harvesting model and resource allocation for SWIPT systems. *IEEE Communications Letters* 19, pp. 2082–2085.
- [56] Chen Y., Zhao N. & Alouini M. (2017) Wireless energy harvesting using signals from multiple fading channels. *IEEE Transactions on Communications* 65, pp. 5027–5039.
- [57] López O.L.A., Alves H., Souza R.D. & Montejo-Sánchez S. (2019) Statistical analysis of multiple antenna strategies for wireless energy transfer. *IEEE Transactions on Communications* 67, pp. 7245–7262.
- [58] Ramezani P. & Jamalipour A. (2020) Two-way dual-hop WPCN with a practical energy harvesting model. *IEEE Transactions on Vehicular Technology* 69, pp. 8013–8017.
- [59] Shi L., Ye Y., Hu R.Q. & Zhang H. (2019) Energy efficiency maximization for SWIPT enabled two-way DF relaying. *IEEE Signal Processing Letters* 26, pp. 755–759.
- [60] Shen S. & Clerckx B. (2021) Beamforming optimization for MIMO wireless power transfer with nonlinear energy harvesting: RF combining versus DC combining. *IEEE Transactions on Wireless Communications* 20, pp. 199–213.
- [61] Ma G., Xu J., Zeng Y. & Moghadam M.R.V. (2019) A generic receiver architecture for MIMO wireless power transfer with nonlinear energy harvesting. *IEEE Signal Processing Letters* 26, pp. 312–316.
- [62] Zeng Y., Clerckx B. & Zhang R. (2017) Communications and signals design for wireless power transmission. *IEEE Transactions on Communications* 65, pp. 2264–2290.
- [63] Maddikunta P.K.R., Hakak S., Alazab M., Bhattacharya S., Gadekallu T.R., Khan W.Z. & Pham Q.V. (2020), Unmanned aerial vehicles in smart agriculture: Applications, requirements and challenges.
- [64] Zeng Y., Wu Q. & Zhang R. (2019) Accessing from the sky: A tutorial on UAV communications for 5G and beyond. *Proceedings of the IEEE* 107, pp. 2327–2375.
- [65] Bi S., Zeng Y. & Zhang R. (2016) Wireless powered communication networks: an overview. *IEEE Wireless Communications* 23, pp. 10–18.
- [66] Zeng Y. & Zhang R. (2015) Full-duplex wireless-powered relay with self-energy recycling. *IEEE Wireless Communications Letters* 4, pp. 201–204.



- [67] Hwang D., Hwang K.C., Kim D.I. & Lee T.J. (2017) Self-energy recycling for RF powered multi-antenna relay channels. *IEEE Transactions on Wireless Communications* 16, pp. 812–824.
- [68] López O.L.A. & Alves H. (2020) Full duplex and wireless-powered communications. In: *Full-Duplex Communications for Future Wireless Networks*, Springer, pp. 219–248.
- [69] Ju H. & Zhang R. (2014) Throughput maximization in wireless powered communication networks. *IEEE Transactions on Wireless Communications* 13, pp. 418–428.
- [70] Isikman A.O., Yuksel M. & Gündüz D. (2017) A low-complexity policy for outage probability minimization with an energy harvesting transmitter. *IEEE Communications Letters* 21, pp. 917–920.
- [71] Alcaraz López O.L., Fernández E.M.G., Souza R.D. & Alves H. (2018) Wireless powered communications with finite battery and finite blocklength. *IEEE Transactions on Communications* 66, pp. 1803–1816.
- [72] Gonçalves L.C., Sebastião P., Souto N. & Correia A. (2020) One step greener: Reducing 5G and beyond networks’ carbon footprint by 2-tiering energy efficiency with CO2 offsetting. *Electronics* 9, p. 464.
- [73] Yang F., Xu W., Liang X. & Lin J. (2017) Joint energy flow and time duration optimization for harvested energy driven WPCN. In: *2017 IEEE Globecom Workshops (GC Wkshps)*, pp. 1–6.
- [74] Bi S., Ho C.K. & Zhang R. (2015) Wireless powered communication: opportunities and challenges. *IEEE Communications Magazine* 53, pp. 117–125.
- [75] Krikidis I., Timotheou S., Nikolaou S., Zheng G., Ng D.W.K. & Schober R. (2014) Simultaneous wireless information and power transfer in modern communication systems. *IEEE Communications Magazine* 52, pp. 104–110.
- [76] Zhou X., Zhang R. & Ho C.K. (2013) Wireless information and power transfer: Architecture design and rate-energy tradeoff. *IEEE Transactions on Communications* 61, pp. 4754–4767.
- [77] Liu L., Zhang R. & Chua K. (2013) Wireless information and power transfer: A dynamic power splitting approach. *IEEE Transactions on Communications* 61, pp. 3990–4001.
- [78] Krikidis I., Sasaki S., Timotheou S. & Ding Z. (2014) A low complexity antenna switching for joint wireless information and energy transfer in MIMO relay channels. *IEEE Transactions on Communications* 62, pp. 1577–1587.
- [79] Timotheou S. & Krikidis I. (2013) Joint information and energy transfer in the spatial domain with channel estimation error. In: *IEEE Online Conference on Green Communications (OnlineGreenComm)*, pp. 115–120.

- [80] Zhao N., Zhang S., Yu F.R., Chen Y., Nallanathan A. & Leung V.C.M. (2017) Exploiting interference for energy harvesting: A survey, research issues, and challenges. *IEEE Access* 5, pp. 10403–10421.
- [81] Li J., Zhao K., Ding X., Shi W. & Miao C. (2021) Operation Scheme of SWIPT Relay System Based on Interference Energy Harvesting. *Arabian Journal for Science and Engineering* 46, pp. 1127–1135. URL: <https://doi.org/10.1007/s13369-020-04638-9>.
- [82] Nasim I. & Kim S. (2019) Adverse impacts of 5G downlinks on human body. In: 2019 SoutheastCon, pp. 1–6.
- [83] He W., Xu B., Gustafsson M., Ying Z. & He S. (2018) RF compliance study of temperature elevation in human head model around 28 GHz for 5G user equipment application: Simulation analysis. *IEEE Access* 6, pp. 830–838.
- [84] Nasim I. & Kim S. (2019) Mitigation of human EMF exposure in downlink of 5G. *Annals of Telecommunications* 74, pp. 45–52.
- [85] Kostoff R.N., Heroux P., Aschner M. & Tsatsakis A. (2020) Adverse health effects of 5G mobile networking technology under real-life conditions. *Toxicology Letters* 323, pp. 35–40.
- [86] Perera T.D.P., Jayakody D.N.K., Chatzinotas S. & Sharma V. (2017) Wireless information and power transfer: Issues, advances, and challenges. In: *IEEE 86th Vehicular Technology Conference (VTC-Fall)*, pp. 1–7.
- [87] Ding X., Sun G., Wang Y., Luo C., Li D., Chen W. & Hu Q. (2019) Cost-minimum charger placement for wireless power transfer. In: *28th International Conference on Computer Communication and Networks (ICCCN)*, pp. 1–9.
- [88] Dai H., Wang X., Liu A.X., Ma H., Chen G. & Dou W. (2018) Wireless charger placement for directional charging. *IEEE/ACM Transactions on Networking* 26, pp. 1865–1878.
- [89] Wang X., Dai H., Wang W., Zheng J., Yu N., Chen G., Dou W. & Wu X. (2020) Practical heterogeneous wireless charger placement with obstacles. *IEEE Transactions on Mobile Computing* 19, pp. 1910–1927.
- [90] Arivudainambi D. & Balaji S. (2018) Optimal placement of wireless chargers in rechargeable sensor networks. *IEEE Sensors Journal* 18, pp. 4212–4222.
- [91] Lu M., Li T., Tan Y. & Wang Z. (2020) Optimization deployed strategy of wireless power beacon based on 5G millimeter wave small cell. In: *IEEE 20th International Conference on Communication Technology (ICCT)*, pp. 462–466.
- [92] Dai H., Wu C., Wang X., Dou W. & Liu Y. (2020) Placing wireless chargers with limited mobility. In: *IEEE Conference on Computer Communications (INFOCOM)*, pp. 2056–2065.

- [93] Dai H., Sun K., Liu A.X., Zhang L., Zheng J. & Chen G. (2020) Charging task scheduling for directional wireless charger networks. *IEEE Transactions on Mobile Computing* , pp. 1–1.
- [94] Liang K., Zhao L., Zheng G. & Chen H. (2019) Non-uniform deployment of power beacons in wireless powered communication networks. *IEEE Transactions on Wireless Communications* 18, pp. 1887–1899.
- [95] Katsidimas I., Kerimakis E. & Nikolettseas S. (2019) Placement optimization in wireless charging systems under the vector model. In: 15th International Conference on Distributed Computing in Sensor Systems (DCOSS), pp. 473–480.
- [96] Katsidimas I., Nikolettseas S. & Raptopoulos C. (2019) Power efficient algorithms for wireless charging under phase shift in the vector model. In: 15th International Conference on Distributed Computing in Sensor Systems (DCOSS), pp. 131–138.
- [97] Zhu Y., Tian X., Chi K., Wen C. & Zhu Y. (2019) Real-time power control of wireless chargers in battery-free body area networks. In: IEEE Global Communications Conference (GLOBECOM), pp. 1–6.
- [98] Zhang C. & Zhao G. (2018) On the deployment of distributed antennas of power beacon in wireless power transfer. *IEEE Access* 6, pp. 7489–7502.
- [99] Dai R., Zhao Y., Chen G., Dou W., Tian C., Wu X. & He T. (2018) Robustly safe charging for wireless power transfer. In: IEEE Conference on Computer Communications (INFOCOM), pp. 378–386.
- [100] López O.L.A., Montejó-Sánchez S., Souza R.D., Papadias C.B. & Alves H. (2021) On CSI-free multi-antenna schemes for massive RF wireless energy transfer. *IEEE Internet of Things Journal* 8, pp. 278–296.
- [101] López O.L.A., Monteiro F.A., Alves H., Zhang R. & Latva-Aho M. (2021) A low-complexity beamforming design for multiuser wireless energy transfer. *IEEE Wireless Communications Letters* 10, pp. 58–62.
- [102] Ju H. & Zhang R. (2014) A novel mode switching scheme utilizing random beamforming for opportunistic energy harvesting. *IEEE Transactions on Wireless Communications* 13, pp. 2150–2162.
- [103] Dai H., Wang X., Xu L., Dong C., Liu Q., Meng L. & Chen G. (2020) Area charging for wireless rechargeable sensors. In: 29th International Conference on Computer Communications and Networks (ICCCN), pp. 1–9.
- [104] Choi K.W., Aziz A.A., Setiawan D., Tran N.M., Ginting L. & Kim D.I. (2018) Distributed wireless power transfer system for Internet of Things devices. *IEEE Internet of Things Journal* 5, pp. 2657–2671.
- [105] Rosabal O.M., López O.L.A., Alves H., Montejó-Sánchez S. & Latva-aho M. (2020) On the optimal deployment of power beacons for massive wireless energy transfer. *IEEE Internet of Things Journal* , pp. 1–1.

- [106] Ha H.T. & Provost S.B. (2013) An accurate approximation to the distribution of a linear combination of non-central chi-square random variables. *REVSTAT–Statistical Journal* 11, pp. 231–254.
- [107] Alfa A.S., Maharaj B.T., Lall S. & Pal S. (2016) Mixed-integer programming based techniques for resource allocation in underlay cognitive radio networks: A survey. *Journal of Communications and Networks* 18, pp. 744–761.
- [108] Gondzio J. (2012) Interior point methods 25 years later. *European Journal of Operational Research* 218, pp. 587–601.
- [109] Boyd S., Boyd S.P. & Vandenberghe L. (2004) *Convex optimization*. Cambridge University Press.
- [110] Bullen P.S. (2013) *Handbook of means and their inequalities*, vol. 560. Springer Science & Business Media.
- [111] Lange M., Zühlke D., Holz O., Villmann T. & Mittweida S.G. (2014) Applications of lp-norms and their smooth approximations for gradient based learning vector quantization. In: *Proceedings of the 22nd European Symposium on Artificial Neural Network (ESANN)*, pp. 271–276.
- [112] Yu W., Taesoo Kwon & Changyong Shin (2010) Joint scheduling and dynamic power spectrum optimization for wireless multicell networks. In: *44th Annual Conference on Information Sciences and Systems (CISS)*, pp. 1–6.
- [113] Steihaug T. (1983) The conjugate gradient method and trust regions in large scale optimization. *SIAM Journal on Numerical Analysis* 20, pp. 626–637.
- [114] Rajakumar R., Dhavachelvan P. & Vengattaraman T. (2016) A survey on nature inspired meta-heuristic algorithms with its domain specifications. In: *International Conference on Communication and Electronics Systems (ICCES)*, pp. 1–6.
- [115] Liu X., Qiu T. & Wang T. (2019) Load-balanced data dissemination for wireless sensor networks: A nature-inspired approach. *IEEE Internet of Things Journal* 6, pp. 9256–9265.
- [116] Mehboob U., Qadir J., Ali S. & Vasilakos A. (2016) Genetic algorithms in wireless networking: techniques, applications, and issues. *Soft Computing* 20, pp. 2467–2501.
- [117] Kulkarni R.V., Venayagamoorthy G.K. & Cheng M.X. (2009) Bio-inspired node localization in wireless sensor networks. In: *2009 IEEE International Conference on Systems, Man and Cybernetics*, pp. 205–210.
- [118] Kulkarni R.V. & Venayagamoorthy G.K. (2011) Particle swarm optimization in wireless-sensor networks: A brief survey. *IEEE Transactions on Systems, Man, and Cybernetics, Part C (Applications and Reviews)* 41, pp. 262–267.
- [119] Yang X.S. (2011) Metaheuristic optimization: algorithm analysis and open problems. In: *International Symposium on Experimental Algorithms*, Springer, pp. 21–32.

- [120] Tsai C.W., Tsai P.W., Pan J.S. & Chao H.C. (2015) Metaheuristics for the deployment problem of WSN: A review. *Microprocessors and Microsystems* 39, pp. 1305–1317.
- [121] Alsayyari A. & Aldosary A. (2019) Path loss results for wireless sensor network deployment in a sparse tree environment. In: *International Symposium on Networks, Computers and Communications (ISNCC)*, pp. 1–6.
- [122] Kurt S. & Tavli B. (2017) Path-loss modeling for wireless sensor networks: A review of models and comparative evaluations. *IEEE Antennas and Propagation Magazine* 59, pp. 18–37.
- [123] Aldossari S.M. & Chen K.C. (2019) Machine learning for wireless communication channel modeling: An overview. *Wireless Personal Communications* 106, pp. 41–70.